



Contents lists available at ScienceDirect

Journal of Fluids and Structures

journal homepage: www.elsevier.com/locate/jfs

Numerical analysis of the hydrodynamic scaling effects for the Wavestar wave energy converter

Christian Windt^{a,b,*}, Josh Davidson^c, John V. Ringwood^a^a Centre for Ocean Energy Research, Maynooth University, Co. Kildare, Ireland^b Leichtweiß-Institute for Hydraulic Engineering and Water Resources, Technische Universität Braunschweig, 38106 Braunschweig, Germany^c Department of Fluid Mechanics, Faculty of Mechanical Engineering Budapest University of Technology and Economics, Hungary

ARTICLE INFO

Article history:

Received 6 May 2020

Received in revised form 27 March 2021

Accepted 7 June 2021

Available online xxx

Keywords:

Scaling effect

Numerical wave tank

Wavestar

RANS

OpenFOAM

ABSTRACT

Scaled model tests are an important step during the research and development of wave energy converters (WECs). While such scaled model tests in physical wave tanks are prone to undesired scaling effects due to e.g. mechanical artefacts and/or fluid effects, numerical wave tanks (NWTs) provide excellent tools for the analysis of WECs across a range of scales, overcoming the limitations of the physical test environment. Simultaneous scaling based on the Froude and Reynolds number is achievable in physical wave tanks only with significant effort, whereas NWTs allow the adjustment of fluid properties, such as viscosity, in an easy manner, thereby catering for Froude and Reynolds similarity. This study exploits the capabilities of a high-fidelity, computational fluid dynamics based, NWT and investigates the hydrodynamic scaling effects for the heaving buoy Wavestar WEC. Various test cases, relevant for WEC applications and with progressively increasing complexity, are considered to develop a comprehensive understanding of the scaling effects. Results show that significant scaling effects occur for the viscous component of the hydrodynamic loads on the WEC hull, while the system dynamics and total (viscous + pressure) loads are relatively unaffected by scaling effects.

© 2021 The Author(s). Published by Elsevier Ltd. This is an open access article under the CC BY license (<http://creativecommons.org/licenses/by/4.0/>).

1. Introduction

In recent years, the public awareness and recognition of global warming and human-induced climate change has fuelled the research and development (R&D) of novel technologies to harness renewable energy sources. Amongst these sources, marine renewable energies, and specifically ocean wave energy, show significant potential to contribute to the global energy mix (de O. Falcão, 2010).

Engineers and researchers are faced with three main challenges during the R&D of wave energy converters (WECs):

- (1) Cost of energy: To be commercially viable, the cost of the produced energy from a WEC must be minimised. The evaluation of the cost of energy, commonly based on the levelised cost of energy (LCoE), relating the overall cost of a device over its lifetime with the provided energy over its lifetime, including expenditures for device manufacturing, deployment, maintenance, and decommissioning.

* Corresponding author at: Centre for Ocean Energy Research, Maynooth University, Co. Kildare, Ireland.
E-mail address: christian.windt.2017@mumail.ie (C. Windt).

- (2) Efficiency: To drive down the LCoE, efficiency of WEC devices, by means of the performance metric *capture width ratio* (Babarit, 2015), can be maximised through hydrodynamic optimisation. In combination with the other subsystems, such as the power take-off (PTO) and energy maximising control systems (EMCSs), optimising the hydrodynamic subsystem of a WEC is required to harvest the maximum energy from each device.
- (3) Survivability: WECs will typically be located at sites exposed to powerful wave climates. When designing a WEC, the expected structural loads in extreme cases, as well as in the power production mode, must be determined to ensure the longevity of the device.

To tackle the above listed challenges, researchers and developers rely heavily on numerical and physical model testing.

1.1. Scaled model testing

Scale model tests in the open ocean, or in physical and numerical wave tanks (NWTs), are commonly used to evaluate and optimise the performance of WECs. From small scale model tests, researchers and developers extrapolate the full scale performance of devices by applying well-known scaling laws, i.e. Froude and Reynolds scaling (Heller, 2011), to scale dimensions of the structure, the considered wave characteristics, and/or the loads exerted on the structure.

Although the applied scaling laws are well established, errors are inherently induced due to the discrepancy between Froude and Reynolds scaling within physical wave tanks, induced by the difficulty to correctly scale fluid viscosity (Veritas, 2000; Schmitt and Elsässer, 2017a). To overcome this issue during physical testing, full scale testing can be considered; however, such tests require extensive capital expenditure and pose difficulties regarding the control and monitoring of the test conditions.

To get a better understanding of hydrodynamic scaling effects, and the implications for performance estimation of the full scale WEC device, NWTs are powerful tools, allowing the analysis of WECs at different scales at virtually no additional cost. Specifically, computational fluid dynamics (CFD) based NWTs, accounting for all relevant hydrodynamic non-linearities, can deliver valuable information on the near flow field around WEC structures and/or the WEC performance, depending on the scale.

1.2. Related studies

In the literature, a number of studies can be found, investigating the effect of different scales during model testing.¹ Wei et al. (2013, 2015) investigate scaling effects on an oscillating wave surge converter (OWSC), for the cases of undamped, damped, and fixed flaps in regular waves. Negligible differences in WEC motion are found for scales between 1/1 and 1/100th. Deviations between the scales are only observed when analysing the vorticity; however, the overall effect of the scale induced deviations are outweighed by the scale independent driving forces of the OWSC.

Also considering an OWSC, Schmitt and Elsässer (2017a) investigate the application of Froude scaling by changing the viscosity of the fluid in a CFD-based NWT, while retaining the dimensions of the structure and the tank across the scales. Comparing angular displacement and power output, small deviations of $\leq 5\%$ are found. The authors also point out the importance of the correct wall treatment and requirements on meshes at different scales for the particular device.

Mundon et al. (2017) perform drag identification tests of the reaction body of a two-body point absorber WEC. In the study, four different scales, between 1/75th – 1/36th, are considered and multiple degrees of freedom (DoFs) are analysed. The authors find good agreement between numerical and experimental results for high Keulegan–Carpenter (KC) and low Reynolds numbers and, furthermore, confirm validity of the scaling laws in such test conditions. For lower KC numbers, the agreement between CFD and experiments diminished and the application of scaling laws fails, leading to overestimation of the drag coefficients.

As part of a series of studies investigating oscillating water columns (OWCs) (Elhanafi, 2016; Elhanafi et al., 2017b,c,e,a; Elhanafi and Kim, 2018; Elhanafi et al., 2018; Shalby et al., 2019; Elhanafi et al. (2017d) study the influence of model scale and air compressibility on the WEC efficiency. With the assumption of incompressible air, scaling effects are negligible; however, analysis at full scale, including compressible air, shows a considerable reduction in efficiency.

Gu et al. (2018) investigate drag, added mass, and radiation damping for the M4 point-absorber device. Considering three different geometries (flat, rounded, and hemispherical bottom), the authors find that, for the larger scale, the drag coefficient shows similar trends, compared to the smaller scale (scaling factor 32), but viscous effects are found to be “somewhat reduced”.

Palm et al. (2018) assess the effects of scale, viscous forces, and drag (viscous and induced) on a moored point-absorber WEC. Simulations at full scale, as well as 1/16th model scale, are performed. Using Reynolds-Averaged Navier Stokes (RANS), Euler, and linear radiation–diffraction (ANSYS AQWA ANSYS, 2020) simulation types, the authors are able to break down the effect of the non-linear mooring response, Froude–Krylov, and viscous forces, as well as the induced drag, non-linear added mass, and the radiation forces on the device dynamics. Concluding, the authors suggest the use of experimental tank tests, together with RANS and Euler simulations, to gain a complete understanding of scale-dependent and scale-independent effects.

¹ A general review of high-fidelity CFD-based NWTs is available in (Windt et al., 2018).

Also considering moored point-absorber type WECs, [Windt et al. \(2019a\)](#) investigate the scaling effects for two different devices in extreme conditions, exposed to focused waves. The authors perform simulations at two different scales (1/1 and 1/10th) where, at the small scale, cases with Froude only, and Froude and Reynolds, scaling are considered. Validation of the numerical model was only possible at small scale. From the simulations, differences of the order of $\mathcal{O}(10\%)$ can be observed between the scales. Furthermore, the results indicate a sensitivity to scaling effects on the considered DoF.

[Dai et al. \(2019\)](#) investigate the hydrodynamic scaling effects on a fixed OWC-type WEC, using experimental and numerical data. Two different scales, with a scaling ratio of 1:3, are considered in the experimental and numerical tests. Good agreement between experimental and numerical data, with an error of the order of $\mathcal{O}(3\%)$ is found when excluding the PTO. Between the scales, an error of the order of $\mathcal{O}(10\%)$ is observed in both the numerical and experimental studies. When including the PTO, which the authors identify as a challenge in itself, the disparity between the physical and numerical wave tank, as well as across the scales, is exacerbated. Ultimately, the authors conclude that the CFD-based NWT is able to reproduce the scaling effects observed in the physical wave tank.

Most recently, [Zabala et al. \(2019\)](#) propose a methodology that employs experimental wave tank tests to validate a CFD-based NWT which will deliver calibration data for a potential flow solver with a drag correction term. The methodology comprises small-scale experimental and CFD-based NWT tests (for validation purposes), as well as full-scale CFD-based NWT tests (for calibration purposes). The authors state that an underlying assumption of this methodology is that a validated small-scale NWT setup is also valid at full-scale. The OWC spar-buoy WEC, for which experimental data is available at 1/16th and 1/120th scale, is used by the authors to prove the proposed concept. For the 1/16th scale model, the body motion and free surface elevation are compared against experimental data; however, only in a qualitative manner. Declaring the 1/16th scale numerical model as validated, the authors perform a numerical heave decay test at 1/120th scale. The qualitative comparison to the experimental data shows good agreement.

1.3. Objectives

From the reviewed literature, two observations can be made:

- (1) CFD-based NWTs generally require experimental validation to ensure the accuracy of the numerical model. However, an existing lack of validated CFD-based NWTs models of the same device across different scales can be observed. Only ([Mundon et al., 2017](#); [Dai et al., 2019](#); [Zabala et al., 2019](#)) include cross-scale validation: While [Mundon et al. \(2017\)](#) only investigate the identification of drag coefficients, [Dai et al. \(2019\)](#) consider a fixed OWC, and [Zabala et al. \(2019\)](#) only provide qualitative validation. There is a need to investigate the scale effects on the performance of a resonating WEC system, in operational conditions, based on validated numerical models.
- (2) CFD-based NWTs provide the capability of by-passing the well known discrepancy between Froude and Reynolds scaling by allowing the alteration of the transport properties of the involved fluid. However, while [Schmitt and Elsässer \(2017a\)](#) only consider scaling of the fluid viscosity and e.g. [Palm et al. \(2018\)](#) only consider scaling of the geometric dimensions, just a single study ([Windt et al., 2019a](#)) can be found investigating the analysis of the scaling effects, including cases considering Froude scaling only, as well as Froude and Reynolds scaling.

This study builds upon ([Windt et al., 2019a](#)), extending the authors' previous work by analysing the hydrodynamic scaling effects for the heaving buoy Wavestar WEC in operational, rather than extreme, conditions, based on a numerical model, validated across scales ([Windt et al., 2020b,a](#)), rather than for only a single scale. In particular, this study considers scaling of the geometric dimensions with full scale fluid viscosities, as well as scaling both the fluid viscosities and geometric dimensions, to analyse the effect of different model scales on the WEC response. The case of scaled geometric dimensions with full scale fluid viscosity represents the typical model setup in a physical wave tank. Hence, this study investigates the hydrodynamic scaling error in such test conditions. For the analysis, three different scales, i.e. 1/20th, 1/5th, and 1/1, are considered, where the CFD-based NWT for the small scale WECs has been successfully validated against experimental reference data for test conditions in [Windt et al. \(2020b,a\)](#). A suite of test cases with increasing complexity is considered, ranging from regular wave-only test cases to wave driven WEC motion in irregular waves.

1.4. Paper outline

The remainder of the paper is organised as follows. Section 2 provides a brief overview of the scaling laws considered throughout this study. Section 3 then details the specific case study considered to analyse the scaling effects. In particular, the section provides information on the Wavestar WEC and the different test cases. The CFD-based NWT used to perform the simulations is presented in Section 4. The results of the test cases for the different scales are presented and discussed in Section 5 and Section 6, respectively. Finally, conclusions are drawn in Section 7.

2. Model scaling

For scaling of the relevant physical properties, the Froude scaling law is applied throughout this study. Froude scaling is based on maintaining a consistent Froude number (see Eq. (1)) between scales, which represents the ratio between

inertia (f_i) and gravity forces (f_g). Hence, when the Froude number remains constant between scales, the ratio between inertial forces and gravitational forces is also constant.

$$Fr = \left(\frac{f_i}{f_g} \right)^{1/2} \quad (1)$$

To achieve Froude scaling, the physical parameters are simply scaled by the corresponding scaling factor, listed in [Table 1](#).

As mentioned in [Section 1](#), special attention must be paid to the scaling of the (kinematic) fluid viscosity, ν , to not only comply with the Froude scaling law but also with the Reynolds scaling law. Reynolds scaling is based on maintaining a consistent Reynolds number (see [Eq. \(2\)](#)) between scales, which represents the ratio between inertia and viscous forces (f_v). Hence, when the Reynolds number remains constant between scales, the ratio between inertial forces and viscous forces is also constant.

$$Re = \frac{f_i}{f_v} \quad (2)$$

In physical wave tanks, viscosity cannot be scaled easily, whereas in CFD-based NWTs the required adjustment can be made simply by changing the transport properties of the fluids involved. Based on the units of ν , i.e. [$\text{m}^2 \text{s}^{-1}$], and the scaling factors given in [Table 1](#), the viscosity can be scaled accordingly:

$$\nu_{MS} = \nu_{FS} \cdot \frac{\sigma^2}{\sqrt{\sigma}}, \quad (3)$$

where the subscript MS refers to model scale and FS refers to full scale.

In this study, three different scales, i.e. 1/1 (FS), 1/5th (MS), and 1/20th (MS), are analysed, such that $\sigma = [1/1, 1/5, 1/20]$, respectively. Furthermore, at 1/5th and 1/20th scale, two cases are considered, representing:

- (1) Froude and Reynolds similarity, i.e. scaling geometric properties, mass, forces, inertial properties, as well as fluid viscosity. Such cases are henceforth referred to as $1/5_{\text{FaR}}$ and $1/20_{\text{FaR}}$.
- (2) Only Froude similarity, i.e. scaling geometric properties, mass, forces, inertial properties, but using full scale fluid viscosity, thereby showing the same properties as small scale physical wave tank test. Such cases are henceforth referred to as $1/5_{\text{F}}$ and $1/20_{\text{F}}$.

3. Case study

For the analysis of hydrodynamic scaling effects, the Wavestar WEC is considered. This section gives a brief overview of the device specifics (see [Section 3.1](#)). The particular numerical reference case is detailed in [Section 3.2](#). Furthermore, this section introduces the different test cases considered for the scaling analysis (see [Section 3.3](#)).

3.1. The Wavestar WEC

The Wavestar WEC consists of several hemispherical hulls, each with a single operational DoF, rotation around a hinge on an fixed structure, rigidly connected to the hull. On a full scale device, the hydraulic PTO system consists of a cylinder, pumping fluid through a generator, with a rated power of 500kW for a device with 20 floaters ([Hals et al., 2015](#)). A photograph of the 1/1 scale model is shown in [Fig. 1\(a\)](#). Experimental test campaigns have been conducted in two different test facilities, at two different scales: Experiments of a 1/5th scale device (see [Fig. 1\(b\)](#)) are documented in ([Jakobsen et al., 2016](#)), while the test campaign of a 1/20th scale device (see [Fig. 1\(c\)](#)) is documented in ([Garcia-Violini et al., 2021](#); [Windt et al., 2020b](#)). The experimental data has been used for independent numerical model validation in ([Windt et al., 2020b,a](#)).

3.2. Numerical WEC model

The current study establishes the numerical model of the 1/20th scale WEC (see [Fig. 2](#)), validated in ([Windt et al., 2020b](#)), as a reference case and applies the scaling laws to this model. The system characteristics are listed in [Table 2](#) for the 1/20th, 1/5th, and 1/1 scale models.

It is important to note that the numerical solvers, solution schemes, and relative discretisation sizes in ([Windt et al., 2020b](#)) (see [Section 4](#)) are consistent with the setting for the numerical 1/5th scale WEC model in ([Windt et al., 2020a](#)), thus the model can be considered validated across scales. Differences between the 1/20th scale model in ([Windt et al., 2020b](#)) and the 1/5th scale model in ([Windt et al., 2020a](#)) occur in terms of the physical properties, such as mass and inertia, which is a characteristic of the underlying physical prototype. The physical WEC model at 1/5th and 1/20th scale are correctly scaled (relative to the 1/1 model) in terms of the floater geometry; however, due to the difference in the mechanical PTO system, as well as in the required sub-structures, the mass and inertial values do not strictly follow scaling laws. The mass of the complete system (floater and PTO), for instance, is adjusted between the physical 1/5th and 1/20th scale model such that the draft of the floater is scaled correctly. As mentioned in [Section 1](#), such difficulties, induced by applying scaling laws, can be bypassed in CFD-based NWTs, allowing the analysis of purely hydrodynamic scaling effects.

Table 1
Froud scaling factors.

Physical parameter	Unit	Scaling factor
Length	[m]	σ
Mass	[kg]	σ^3
Force	[N]	σ^3
Torque	[Nm]	σ^4
Acceleration	[m s ⁻²]	1
Time	[s]	$\sqrt{\sigma}$
Pressure	[Pa]	σ

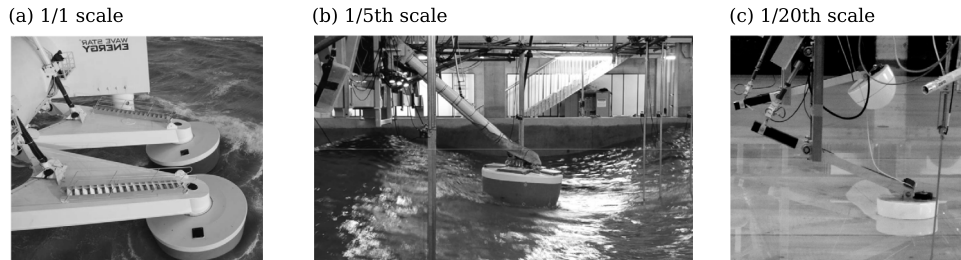


Fig. 1. Photographs of the Wavestar WEC at different scales. (a) Full scale (adopted from Tougaard, 2015); (b) 1/5th scale at the University of Plymouth (adopted from Jakobsen, 2014); (c) 1/20th scale at Aalborg University (adopted from Windt et al., 2020b).

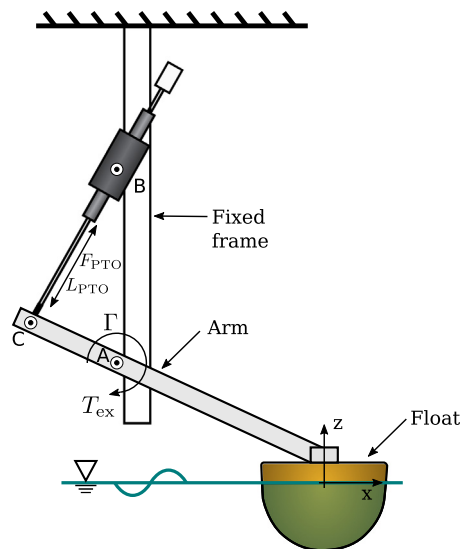


Fig. 2. Schematic of the numerical WEC model, inspired by the 1/20th scale model in (Garcia-Violini et al., 2021) and (Windt et al., 2020b).

Further note that the experimental data sets, used for the validation in (Windt et al., 2020b,a), include measurements of the WEC motion, the total hydrodynamic force acting on the WEC, the pressure at discrete locations on the WEC hull and the free surface elevation at discrete locations throughout the wave tank. Although it is not feasible to measure the entire flow field in the wave tank, the good agreement between the numerical model and the range of measured quantities suggests that no large deviations between the flow field in the wave tank and the numerical model are expected.

3.3. Test cases

Similarly to the validation studies in (Windt et al., 2020a,b), the present analysis of the hydrodynamic scaling effects for the Wavestar WEC follows an incremental approach:

- Initially, to investigate the influence of scaling on the incident waves, wave-only test cases are considered (see Section 3.3.1).
- To introduce wave–structure interaction, but still keep the complexity of the model relatively low, wave excitation force tests are examined (see Section 3.3.2).

Table 2

Physical properties of the 1/20th, 1/5th, and 1/1 scale Wavestar model. The hinge notation can be extracted from Fig. 2.

		1/20 _{FaR} (1/20 _F)	1/5 _{FaR} (1/5 _F)	1/1
Hinge A:				
x	[m]	−0.449	−1.796	−8.98
y	[m]	0.000	0.000	0.00
z	[m]	0.232	0.928	4.64
Hinge B:				
x	[m]	−0.449	−1.796	−8.98
y	[m]	0.000	0.000	0.00
z	[m]	0.642	2.568	12.84
Hinge C:				
x	[m]	−0.636	−2.544	−12.72
y	[m]	0.000	0.000	0.00
z	[m]	0.303	1.212	6.06
Centre of Mass (CoM):				
x	[m]	−0.053	−0.212	−1.06
y	[m]	0.000	0.000	0.00
z	[m]	0.108	0.432	2.16
Mass (Float & Arm)	[kg]	4.10	262.40	32800
Inertia (Float & Arm)	[kg m ²]	0.434	444.42	1388800
Floater diameter (at SWL)	[m]	0.256	1.02	5.12
Submergence (in equilibrium)	[m]	0.110	0.44	2.20
Water depth <i>d</i>	[m]	0.900	3.60	18.00

Table 3

Characteristics of the regular and irregular wave.

	$H (H_s)$	$T (T_p)$	$f (f_p)$	$\lambda (\lambda_p)$	$H/\lambda (H_s/\lambda_p)$
1/1	1.20 m	6.26 s	0.16 Hz	58.60 m	0.02
1/5 _{FaR} (1/5 _F)	0.24 m	2.80 s	0.36 Hz	11.72 m	0.02
1/20 _{FaR} (1/20 _F)	0.06 m	1.40 s	0.71 Hz	2.93 m	0.02
Resonance	H	T	f	λ	H/λ
1/1	1.20 m	3.72 s	0.27 Hz	21.60 m	0.06
1/5 _{FaR} (1/5 _F)	0.24 m	1.66 s	0.60 Hz	4.30 m	0.06
1/20 _{FaR} (1/20 _F)	0.06 m	0.83 s	1.20 Hz	1.08 m	0.06

- To develop a preliminary understanding of the numerical model capability in replicating the system dynamics, free decay tests are investigated (see Section 3.3.3).
- Progressively increasing the complexity of the test cases, forced oscillation tests are studied (see Section 3.3.4)
- Finally, wave-induced motion tests, under regular and irregular wave excitation, are analysed (see Section 3.3.5).

3.3.1. Wave-only tests

For the wave-only test cases, the waves propagate through the tank undisturbed. The long crested plane waves, considered in the present study, allow simulation in a two-dimensional domain, since such waves are invariant in the lateral direction. For scale analysis, both a regular and irregular wave trains are considered. For the regular wave case, two different wave steepnesses are considered, where the wave period of the steeper wave is chosen based on the resonance period of the WEC device.

The characteristics of the waves, i.e. (significant) wave height, $H (H_s)$, (peak) wave period, $T (T_p)$, (peak) wave frequency, $f (f_p)$, (peak) wave length, $\lambda (\lambda_p)$, and wave steepness $H/\lambda (H_s/\lambda_p)$ are listed in Table 3. For the regular and irregular wave trains, simulations are run for 20 and 100 (peak) periods, respectively. Free surface elevation measurements are extracted at four different locations, depicted in Fig. 4.

3.3.2. Wave excitation tests

During the wave excitation force tests, the WEC is locked in its equilibrium position, while being exposed to the regular and irregular wave train. The wave excitation torque, T_{ex} , about pivot point A (see Fig. 2), is monitored and compared across the scales. The wave excitation torque T_{ex} can be easily extracted from each CFD simulation during post-processing, and the pressure and viscous shear force components can be separately quantified. Note that, during physical experiments, the translational force acting along the PTO axis would be the most direct way to measure wave excitation, with no means of distinguishing the separate contributions from the pressure and viscous shear forces.

Table 4
Characteristics of the Multi-frequency excitation input.

	Frequency range	Force amplitude
1/1	[0.02, 1.07] Hz	80 000 N
1/5 _{FaR} (1/5 _F)	[0.06, 2.39] Hz	640 N
1/20 _{FaR} (1/20 _F)	[0.11, 4.77] Hz	10 N

3.3.3. Free decay test

For the free decay tests, the initial position of the body is displaced by 2° from equilibrium, resulting in an exponentially decaying oscillation back to its rest state. The WEC motion and the hydrodynamic force on the WEC hull are monitored and compared across scales. The motion of the WEC is measured from the displacement of the PTO translator shaft, L_{PTO} .

3.3.4. Forced oscillation tests

The forced oscillation tests involve using the PTO system to apply a defined input force, F_{PTO} , on the WEC, without any input waves in the tank. The resulting WEC motion is monitored and compared across the scales. Two different types of input force signals can be distinguished:

Single-frequency excitation: For the single-frequency excitation cases, a simple sinusoidal force signal is used to drive the system. The force amplitude is set to 5N (at 1/20th scale) and the frequency corresponds to the wave frequency in Table 3. Simulations are run for 20 oscillation periods.

Multi-frequency excitation: The multi-frequency excitation experiments, realised through up-chirp force signals, are commonly performed for system identification purposes (Ringwood et al., 2016; Davidson et al., 2016; Garcia-Violini et al., 2021). The input force is defined as a linear frequency sweep with a fixed amplitude and the characteristics listed in Table 4.

3.3.5. Wave-induced WEC motion tests

Finally, for the wave-induced WEC motion tests, the WEC is exposed to the incident regular and irregular wave trains. The motion and hydrodynamic forces on the WEC hull are monitored and compared across the scales.

For the case of the regular wave excitation, two cases are considered. One with a regular wave period of 6.26 s (at 1/1 scale) and an additional case with a regular wave period of 3.72 s (at 1/1 scale), see Table 3. The latter wave period reflects the resonant period of the device and is motivated by WEC analysis under controlled conditions, where the WEC dynamics are pushed towards resonance with the incident wave, thereby enhancing WEC motion and power production. It is well known that, due to the enhanced WEC motion, hydrodynamic non-linear effects are introduced (Davidson et al., 2019; Giorgi and Ringwood, 2017), which may further induce hydrodynamic scaling effects.

4. Numerical wave tank

The open-source CFD toolbox OpenFOAM, version 4.1, is used to set up the CFD-based NWT, following the validation studies presented in (Windt et al., 2020a,b).

4.1. Governing equations

In OpenFOAM, the incompressible (and isothermal) RANS equations,² describing the conservation of mass (Eq. (4)) and momentum (Eq. (5)), are solved using the finite-volume method (Weller et al., 1998).

$$\nabla \cdot \mathbf{u} = 0 \quad (4)$$

$$\frac{\partial(\rho \mathbf{u})}{\partial t} + \nabla \cdot (\rho \mathbf{u} \mathbf{u}) = -\nabla p + \nabla \cdot (\mu \nabla \mathbf{u}) + \rho \mathbf{f}_b, \quad (5)$$

where t denotes time, \mathbf{u} the fluid velocity, p the fluid pressure, ρ the fluid density, $\mu = \nu \rho$ the dynamic viscosity, and \mathbf{f}_b the external forces such as gravity.

The pressure-velocity coupling is solved using the PIMPLE algorithm (Holzmann, 2016), blending the semi-implicit method for pressure-linked equations (SIMPLE) (Patankar and Spalding, 1972) and the pressure-implicit split-operator (PISO) (Issa, 1986).

To account for the two phase flow of air and water, the volume of fluid (VoF) method, proposed in (Hirt and Nichols, 1981), is employed. Defining a volume fraction, α , the properties of the fluid mixture (density and viscosity) can be expressed as:

$$\rho = \alpha \rho_{\text{water}} + (1 - \alpha_{\text{VF}}) \rho_{\text{air}}, \quad (6)$$

² Alternatives to RANS modelling include, e.g., DNS, DES, LES, Euler or potential flow simulations (see Davidson and Costello, 2020 for a review of simulation methods alternative to RANS). While DNS, DES, or LES are computationally too expensive, Euler and potential flow simulations would completely neglect viscosity, which would significantly compromise the purpose of this study.

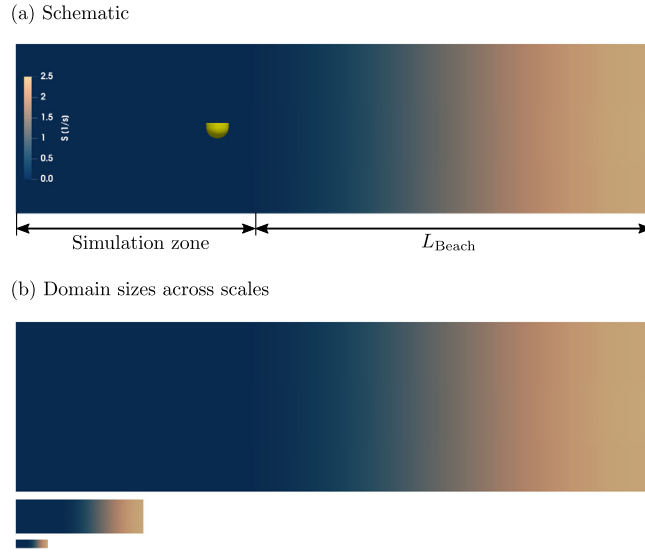


Fig. 3. Side view of the computational domain: Screen shot of the \mathbf{S} field.

and

$$\mu = \alpha \mu_{\text{water}} + (1 - \alpha) \mu_{\text{air}}. \quad (7)$$

In OpenFOAM, the transport equation for α follows:

$$\frac{\partial \alpha}{\partial t} + \nabla \cdot (\mathbf{u}\alpha) + \nabla \cdot [\mathbf{u}_r \alpha (1 - \alpha)] = 0, \quad (8)$$

where \mathbf{u}_r is the relative velocity between the water and air phases (Berberović et al., 2009). Boundedness of the transport equation is achieved through the multi-dimensional limiter for explicit solutions (MULES) (Rusche, 2002).

The body motion, induced by the incident wave or external force, is solved via Newton's 2nd law of motion, by the *sixDoFRigidBodyMotionSolver* in OpenFOAM. The motion solver provides a set of restraint functions, facilitating the numerical representation of the translational PTO. One of the existing restraint functions is modified for the forced oscillation tests, allowing any arbitrary force signal to be input and applied to the WEC motion. The successful use of the motion solver to replicate a linear actuator type PTO system is demonstrated by Penalba et al. (2018), Windt et al. (2020a,b). The resulting body motion is accommodated in the numerical domain through mesh morphing by means of the spherical linear interpolation (SLERP) algorithm. Finally, based on (Windt et al., 2020a,b), laminar flow conditions are assumed for all simulations.

4.2. Numerical wave generation and absorption

Several methods are available in OpenFOAM to implement wave generation and absorption (Miquel et al., 2018; Windt et al., 2019b). A static boundary method, proposed by Higuera et al. (2013), for wave generation, together with a numerical beach, proposed by Schmitt and Elsaesser (2015), for wave absorption, is used in the present numerical model. For the numerical beach, introducing the dissipation term, $\mathbf{S}\rho\mathbf{u}$, to the RANS momentum equation (5), yields:

$$\frac{\partial(\rho\mathbf{u})}{\partial t} + \nabla \cdot (\rho\mathbf{u}\mathbf{u}) = -\nabla p + \nabla \cdot (\mu\nabla\mathbf{u}) + \rho\mathbf{f}_b + \mathbf{S}\rho\mathbf{u} \quad (9)$$

The variable field \mathbf{S} controls the dissipation strength, with a value of zero in the simulation zone, which then gradually increases, following an analytical expression, over a defined beach length, L_{Beach} , to a maximum damping factor, S_{max} (see Fig. 3). The specific combination of wave generation and absorption methods can deliver good free surface elevation fidelity with minimal wave reflection and low cell counts.

The optimal beach length and the maximum damping factor within the numerical beach S_{max} are determined by Windt et al. (2020b) and set to 4.5 m and 2.5 s^{-1} at 1/20th scale, respectively. A screen shot of the \mathbf{S} field at 1/20th scale is shown in Fig. 3. Table 5 lists the values for L_{Beach} and S_{max} for all scales.

4.3. Computational domain

The same computational domain is used for all the different test cases outlined in Section 3.3. Fig. 4 show the side (a) and top view (b) of the numerical domain, including the applied boundary conditions. The relevant dimensions of the

Table 5
Characteristics of the numerical beach across scales.

	$1/20_{FaR}$ ($1/20_F$)	$1/5_{FaR}$ ($1/5_F$)	1/1
L_{Beach} [m]	4.5	18.0	90.0
S_{max} [s^{-1}]	2.50	1.25	0.56

Table 6
Dimensions of the numerical wave tank across scales.

		$1/20_{FaR}$ ($1/20_F$)	$1/5_{FaR}$ ($1/5_F$)	1/1
h_{Tank}	[m]	1.80	7.20	36.0
w_{Tank}	[m]	3.25	13.00	65.0
l_{Tank}	[m]	6.81	27.24	136.2
l_{Device}	[m]	2.16	8.64	43.2
d	[m]	0.90	3.60	18.00
l_{WP1}	[m]	0.45	1.80	9.0
l_{WP2}	[m]	0.20	0.80	4.0
l_{WP4}	[m]	0.86	3.44	17.2

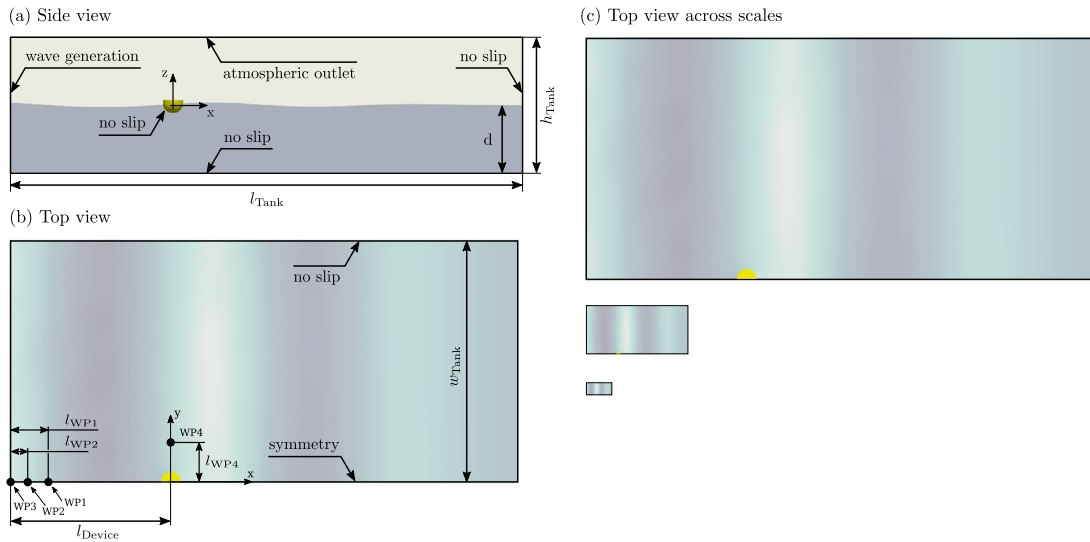


Fig. 4. Schematic of the numerical wave tank: Side view (a) and top view (b).

computational domain at the three different scale are listed in Table 6. To reduce the overall cell count, the symmetry of the problem is exploited. A symmetry boundary condition is employed in the xz -plane, where x points in the wave propagation direction, and z away from the tank floor (see Fig. 4).

The choice of the spatial and temporal discretisation sizes follows (Windt et al., 2020a,b). Spatially, the interface region in the simulation zone (see Fig. 5) and region around the body are discretised with cells of a (vertical) size of 10 cells per wave height and a maximum aspect ratio of 4 in the horizontal and lateral direction, resulting in 116 cells per λ . The overall cell count is ~ 1.7 M cells. For the temporal discretisation, a fixed time step size of 0.001 s is used at the 1/20th scale and scaled according to Froude scaling. The analysis of the influence of the time step scaling on some example results is shown in Appendix. A screen shot of the discretisation in the xz -plane is shown in Fig. 5.

4.4. Flow conditions

When modelling WECs in high-fidelity, CFD-based, modelling frameworks, the questions arises as to whether or not turbulence effects must be considered. In fact, the necessity and methodology of modelling turbulence (by means of industry-standard turbulence models) is an active field of research (Folley, 2016). When setting up an NWT model, CFD engineers are faced with the choice of a particular (RANS) turbulence model, the initial turbulence intensity for model initialisation, as well as an appropriate discretisation of the boundary layer in the vicinity of the WEC structure. For the choice of the particular RANS turbulence model, no industry-standard guidelines have been formulated yet (Folley, 2016; Windt et al., 2018). Regarding the correct wall treatment, generally, the well-known y^+ criterion for the use of standard

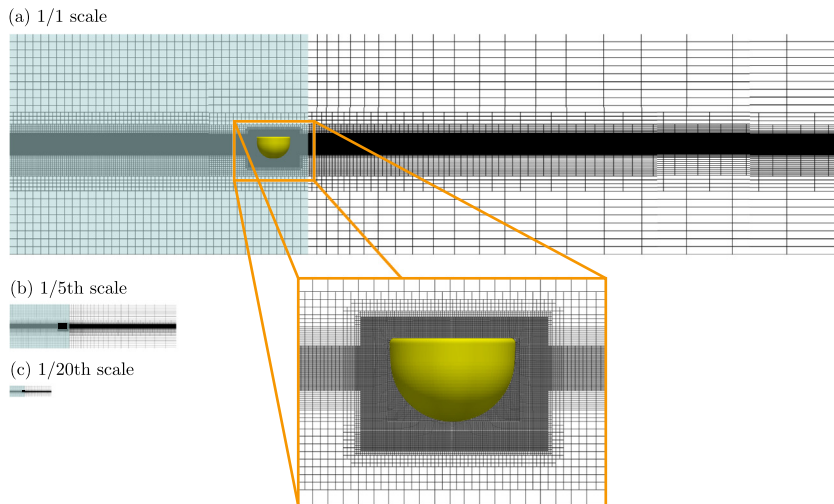


Fig. 5. Screen shot of the computational mesh in the xz -plane. The simulation zone, in which the damping factor $S = 0$, is highlighted in blue. (For interpretation of the references to colour in this figure legend, the reader is referred to the web version of this article.)

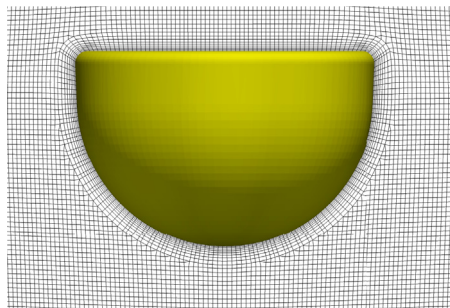


Fig. 6. Screen shot of the computational mesh in the xz -plane in the vicinity of the WEC structure.

wall functions ($30 < y^+ < 300$) can be employed to verify the spatial discretisation within the NWT. However, as pointed out by [Schmitt and Elsässer \(2017a\)](#), for the oscillating flow around WEC structures, no single mesh can be found that obeys the condition on y^+ over an entire wave cycle or sea state. As discussed by [Davidson and Costello \(2020\)](#), the unresolved challenge in applying turbulence models to WEC applications is that it is a transient problem, such that both the WEC hull and the surrounding fluid are oscillating, thus it is questionable whether the boundary layer has time to fully develop, in addition to the fact that the y^+ value is constantly changing and frequently equals zero.

All of the above factors, and the associated uncertainty, lead to the assumption of laminar flow conditions to be applied throughout this study. This assumption is backed by the successful validation of the 1/5th ([Windt et al., 2020a](#)) and 1/20th ([Windt et al., 2020b](#)) scale Wavestar model, under the assumption of laminar flow conditions in the NWT model, using wave field, floater position, wave excitation force and pressure data.

To get an understanding of the potential differences between the numerical results under the assumption of laminar and turbulent flow conditions, results of the wave-induced WEC motion test under regular wave excitation are compared. Here, only the smallest scale, i.e. $1/20_{\text{Farth}}$, is considered since, generally, turbulence effects are prevalent at smaller scales. For the cases assuming turbulent flow conditions, the $k - \omega$ SST turbulence model, proposed by [Menter \(1992b,a, 1994, 1997\)](#), is employed together with standard wall functions. The initial turbulence intensity is set to 5% and, throughout the course of the simulation, a maximum $y^+ \approx 500$ is achieved. For reference, [Fig. 6](#) shows the spatial discretisation in the vicinity of the WEC structure.

[Fig. 7](#) shows the comparison of the WEC displacement, as well as the total wave excitation torque and its viscous component on the WEC hull. From the results in [Fig. 7](#), relatively small differences can be observed between the laminar and turbulent case for the WEC displacement ([Fig. 7\(a\)](#)) and the total wave excitation torque ([Fig. 7\(b\)](#)), indicating that the effect of turbulence modelling on these quantities is relatively small. In the light of the successful validation of the small scale Wavestar model under the assumption of laminar flow conditions, and the previously discussed uncertainty when modelling turbulence, the results in [Fig. 7\(a\)](#) and (b) support the assumption of laminar flow conditions throughout this study. [Fig. 7\(c\)](#) shows the viscous component of the wave excitation torque, exhibiting relatively large differences between

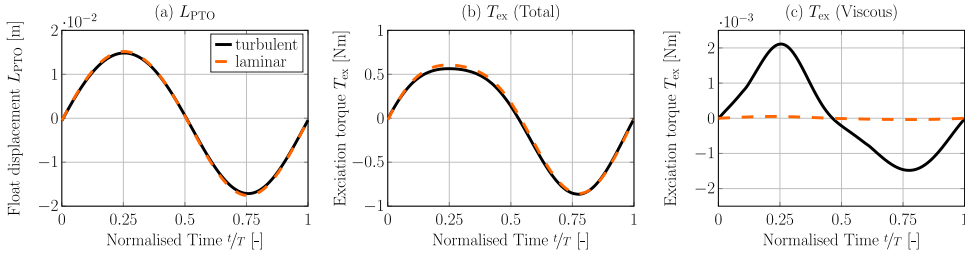


Fig. 7. Time trace of the phase averaged (a) WEC displacement, (b) total hydrodynamic torque, and (c) viscous component of the total hydrodynamic torque at $1/20_{\text{FaR}}$ scale for the case of laminar and turbulent flow assumptions.

Table 7

Kinematic fluid viscosities for the considered model scales.

Scale	Water viscosity [$\text{m}^2 \text{s}^{-1}$]	Air viscosity [$\text{m}^2 \text{s}^{-1}$]
1/1	1.00E-6	1.48E-5
$1/5_{\text{F}}$	1.00E-6	1.48E-5
$1/5_{\text{FaR}}$	8.94E-8	1.32E-6
$1/20_{\text{F}}$	1.00E-6	1.48E-5
$1/20_{\text{FaR}}$	1.12E-8	1.65E-7

the laminar and turbulent case. Acknowledging the similarity between viscosity and the effects of turbulence, i.e. increased transport and dissipation, it is expected that the turbulent case will result in larger values of viscous excitation torque. Overall, however, it is noted that the order of magnitude of the viscous torque component is (even in the turbulent case) two times smaller than the total excitation torque. The effect of the increased viscous torque on the WEC displacement and the total excitation torque is, hence, negligible.

4.5. Viscosity

To achieve Froude and Reynolds scaling in the $1/5_{\text{FaR}}$ th and $1/20_{\text{FaR}}$ th scale case, the fluid viscosity has to be scaled, using the relationship shown in (3). For the $1/5_{\text{F}}$ th and $1/20_{\text{F}}$ th scale, fluid viscosities of the 1/1 scale case are used. Table 7 lists the different fluid viscosities, of water and air, for all scales.

5. Results

This section presents the results for the different test cases introduced in Section 3.3. All results are compared at full scale, requiring scaling of the $1/5$ th and $1/20$ th results, using the scaling factors in Table 1.

The results are analysed qualitatively and quantitatively. For the former, plots of the relevant quantities are shown across the scales. For the quantitative comparison, the normalised root-mean square deviation (nRMSD) is evaluated, following:

$$\text{nRMSD}_{kl} = \sqrt{\frac{\sum_{i=1}^n [y_k(i) - y_l(i)]^2}{n}} \frac{100\%}{\mathcal{N}}, \quad (10)$$

where n is the signal length in terms of the number of sampling points, y denotes the considered quantity (e.g. surface elevation, excitation torque, etc.), and the subscript k and l indicate a specific scale, i.e. 1/1, $1/5_{\text{F}}$, $1/5_{\text{FaR}}$, $1/20_{\text{F}}$, $1/20_{\text{FaR}}$. The normalisation factor, \mathcal{N} , is defined as $\mathcal{N} = \max(y_{(1/1)}) + |\min(y_{(1/1)})|$.

Following the above calculations, the ‘deviation matrix’ (e.g. Table 8) can be calculated, showing the differences between all combinations of the different scales. Comparing the results between 1/1, $1/5_{\text{FaR}}$, and $1/20_{\text{FaR}}$, no differences are expected between the scales, since both Froude and Reynolds scaling are obeyed and any deviations can be attributed to numerical artefacts. Assuming correct scaling between 1/1 and the FaR scales and comparing the results between $1/5_{\text{FaR}}$ and $1/5_{\text{F}}$, as well as $1/20_{\text{FaR}}$ and $1/20_{\text{F}}$, potential scaling errors due to the mismatch between theoretically correct and physically feasible scaling can be seen. Those results are highlighted in red in the ‘deviation matrix’.

5.1. Wave-only tests

Following the incremental procedure outlined in Section 3.3, first, the wave-only cases are compared across the scales.

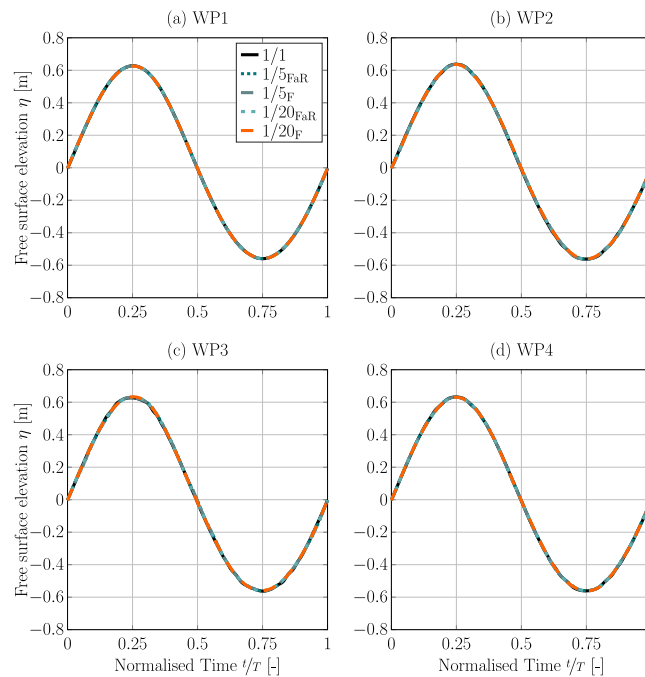


Fig. 8. Time trace of the phase averaged free surface elevation.

Table 8

nRMSD [%] between the scales for the free surface elevation measured at WP4.

	1/5 _F	1/5 _{FaR}	1/20 _F	1/20 _{FaR}
1/1	0.24	0.24	0.24	0.24
1/5 _F		0.00	0.15	0.15
1/5 _{FaR}			0.15	0.15
1/20 _F				0.00

5.1.1. Regular waves

Starting with regular waves, Figs. 8(a)–(d) show the phase averaged time traces of the free surface elevation at the four wave probes WP1–WP4,³ respectively (the wave probe locations are marked in Fig. 4). Visual inspection of the results allows a qualitative comparison, indicating that negligible differences can be observed between the scales at all wave probe locations.

Table 8 shows the ‘deviation matrix’ for the results at wave probe WP4, with all symmetric entries blanked out. Overall, relatively small deviations ($< 0.25\%$) can be observed between the various scales. For the regular wave-only case, virtually no difference ($\text{nRMSD} < 0.01\%$) between $1/5_{\text{FaR}}$ and $1/5_{\text{F}}$, as well as $1/20_{\text{FaR}}$ and $1/20_{\text{F}}$, are found, highlighting the negligible effect of fluid viscosity for this particular case. Accordingly, the same deviation of 0.24% is visible between all small scales and the 1/1 scale. Expecting no difference between the 1/1 and the FaR scales, due to the obedience of Froude and Reynolds scaling, the observed error likely stems from numerical artefacts.

In addition to the free surface elevation data, the velocity profiles underneath wave troughs and crests can be investigated. Extracting the velocity data at the intended device location during the wave-only test cases, Figs. 9(a) and (b) show the resulting velocity profiles underneath a wave trough and crest, respectively. The corresponding ‘deviation matrices’ are shown in Tables 9 and 10 for the wave trough and crest, respectively.

The observed results for the velocity profiles are consistent with the results for the free surface elevation, whereby negligible differences can be observed across the scales. Largest errors of 0.24% (underneath the trough) and 0.14% (underneath the crest) can be observed when comparing the 1/1 and $1/20_{\text{FaR}}$ scale.

5.1.2. Regular waves – resonance

Similar to Fig. 8, Fig. 10(a)–(d) show the phase averaged time traces of the free surface elevation at the four wave probes WP1–WP4 for the case of the regular wave for resonance conditions. The corresponding ‘deviation matrix’ for the free surface elevation measured at WP4 is shown in Table 11.

³ Note that, since 2D domains are considered for the wave-only tests, the position of WP4 in the y -direction is shifted to 0, while, for the 3D case, the position of WP4 in the y -direction is l_{WP4} .

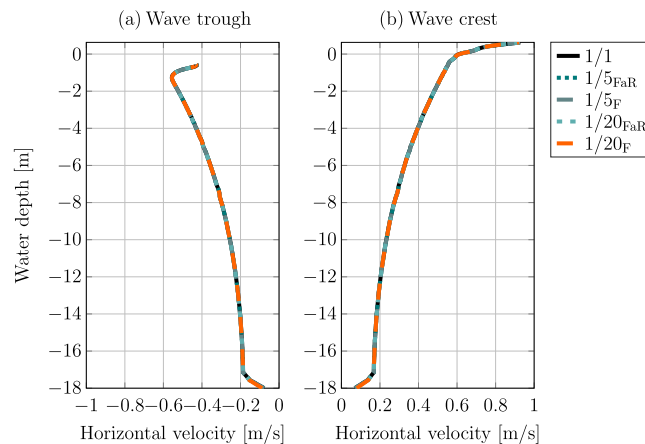


Fig. 9. Profiles of the horizontal velocity along the water column for (a) the wave trough and (b) the wave crest.

Table 9

nRMSD [%] between the scales for the horizontal wave velocity underneath a wave trough.

	1/5 _F	1/5 _{FaR}	1/20 _F	1/20 _{FaR}
1/1	0.04	0.05	0.23	0.24
1/5 _F		0.00	0.21	0.21
1/5 _{FaR}			0.21	0.21
1/20 _F				0.04

Table 10

nRMSD [%] between the scales for the horizontal wave velocity underneath a wave crest.

	1/5 _F	1/5 _{FaR}	1/20 _F	1/20 _{FaR}
1/1	0.04	0.04	0.13	0.14
1/5 _F		0.01	0.11	0.12
1/5 _{FaR}			0.11	0.12
1/20 _F				0.05

Table 11

nRMSD [%] between the scales for the free surface elevation measured at WP4.

	1/5 _F	1/5 _{FaR}	1/20 _F	1/20 _{FaR}
1/1	0.17	0.16	0.24	0.20
1/5 _F		0.01	0.16	0.15
1/5 _{FaR}			0.16	0.15
1/20 _F				0.09

The results indicate that the scaling effects are consistent for the wave only case even when considering waves of varying steepness. The agreement between the free surface elevation, as well as the velocity profiles, across all scales and for different wave conditions allows any deviations in the following test cases to be attributed to wave–structure interaction.

5.1.3. Irregular waves

For the irregular waves, the deviation across the scales is analysed in both the time and frequency domains. By way of example, Fig. 11(a) shows the time traces for the free surface elevation (measured at WP4) at 1/1 scale. Based on the free surface elevation time traces, the spectral density function (SDF) is plotted in Fig. 11(b). From the plot in Fig. 11(b), no qualitative difference can be observed between scales. The results for the irregular waves are therefore consistent with the results for the regular wave.

Tables 12 and 13 show the nRMSD between scales for the free surface elevation, measured at WP4, and the according nRMSD for the SDF, respectively. Overall, similar deviations are calculated for the irregular waves, compared to the regular waves, for both the free surface elevation (nRMSD < 0.25%) and the SDF (nRMSD << 0.05%).

In particular, comparing the nRMSD from the time traces between the 1/1 and FaR scales, similar deviations, as for the regular wave case, can be observed. This is expected since the underlying numerical artefacts inducing the deviations

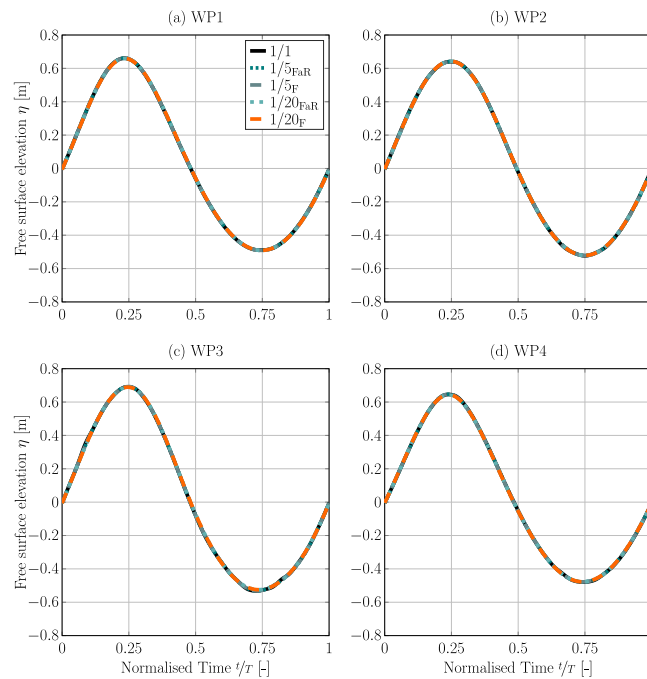


Fig. 10. Time trace of the phase averaged free surface elevation.

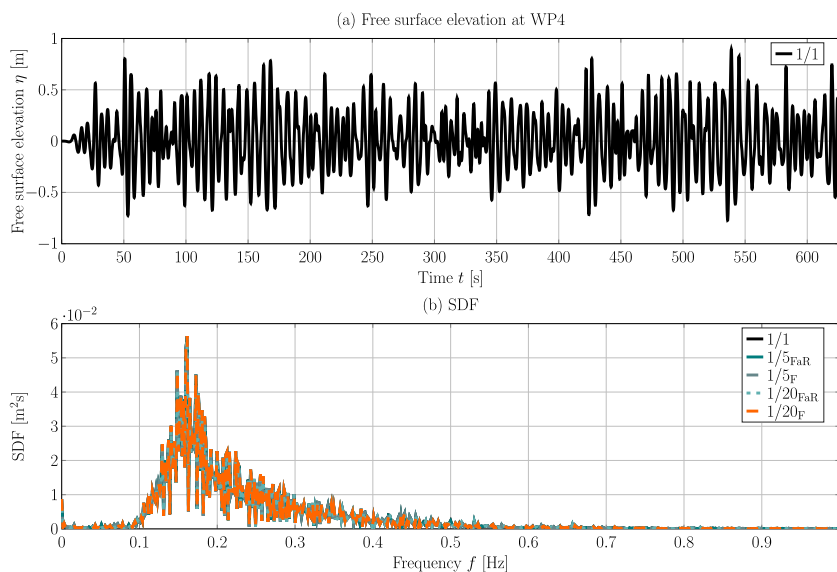


Fig. 11. (a) Time trace of the irregular wave for the 1/1 scale measured at WP4; (b) SDF for all scales based on the free surface elevation measured at WP4.

are believed to be similar for the two cases. For the $1/5_{FaR}$ and $1/5_F$ cases, as well as the $1/20_{FaR}$ and $1/20_F$ scales, deviations of only up to 0.07% are shown, indicating a slightly larger, compared to the regular wave-only case, but still negligible influence of viscosity.

5.2. Wave excitation tests

Introducing wave–structure interaction, wave excitation force tests are first considered for regular and irregular waves.

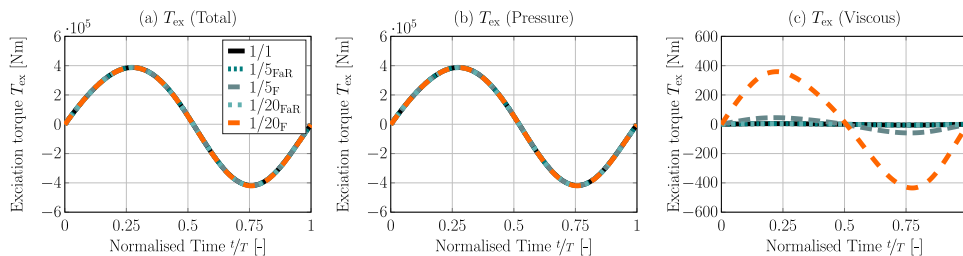


Fig. 12. Time trace of the phase averaged excitation torque.

Table 12
nRMSD [%] between the scales for the free surface elevation measured at WP4.

	1/5 _F	1/5 _{FaR}	1/20 _F	1/20 _{FaR}
1/1	0.16	0.16	0.20	0.19
1/5 _F		0.01	0.14	0.12
1/5 _{FaR}			0.14	0.12
1/20 _F				0.07

Table 13
nRMSD [%] between the scales for the SDF.

	1/5 _F	1/5 _{FaR}	1/20 _F	1/20 _{FaR}
1/1	0.03	0.03	0.04	0.03
1/5 _F		0.00	0.03	0.03
1/5 _{FaR}			0.03	0.02
1/20 _F				0.01

Table 14
nRMSD [%] between the scales for the total excitation torque.

	1/5 _F	1/5 _{FaR}	1/20 _F	1/20 _{FaR}
1/1	0.07	0.07	0.16	0.13
1/5 _F		0.02	0.20	0.19
1/5 _{FaR}			0.21	0.19
1/20 _F				0.11

5.2.1. Regular waves

Figs. 12(a)–(c) show the total, phase averaged, wave excitation torque and the contributing components due to pressure and viscous shear, respectively.

An inspection of the force magnitudes in Fig. 12(a)–(c) reveals a clear dominance of pressure induced wave excitation torque on the WEC hull, with torques of the order of $\mathcal{O}(1 \times 10^5 \text{ N m})$ for the pressure component and $\mathcal{O}(1 \times 10^2 \text{ N m})$ for the viscous component. Furthermore, for the pressure component and, thus, the total wave excitation torque, no qualitative difference can be observed between the scales. Conversely, the viscous component of T_{ex} shows significant difference between the scales, where the viscous shear forces for the 1/20_F scale are larger, compared to the 1/1 scale.

The qualitative analysis is underlined by the quantitative analysis, based on the nRMSD, listed in Tables 14–16. The values of the nRMSD for the total T_{ex} , and its pressure component, show similar values which are, in fact, in accordance with the nRMSD values calculated for the regular wave-only case, i.e. nRMSD < 0.25%. Conversely, for the viscous component of T_{ex} , nRMSD values of up to $\sim 2900\%$ are calculated. For the deviation between the 1/5_{FaR} and 1/5_F, a nRMSD of 352% is calculated, highlighting larger viscous forces in the 1/5_F case. This is expected since the fluid viscosity at 1/5_F is larger (by a factor of 11, see Table 7), compared to the 1/5 scale. Similarly, the deviation between the 1/20_{FaR} and 1/20_F scale shows a deviation of 2912% which can, again, be attributed to a larger fluid viscosity (by a factor of 89, see Table 7) at 1/20_F, compared to the 1/20_{FaR} scale. For the 1/1, 1/5_{FaR}, and 1/20_{FaR} cases, the nRMSD falls into the same range as for the total T_{ex} and its pressure component, i.e. < 0.25%.

Even though significant deviations can be observed for the viscous components of T_{ex} , the comparison between scales for the total T_{ex} is unaffected by these deviations, being dominated by the pressure component, which may be specific to the investigated case. If the problem at hand is dominated by viscous forces, more significant deviations between the total T_{ex} at various scales may be expected.

5.2.2. Irregular waves

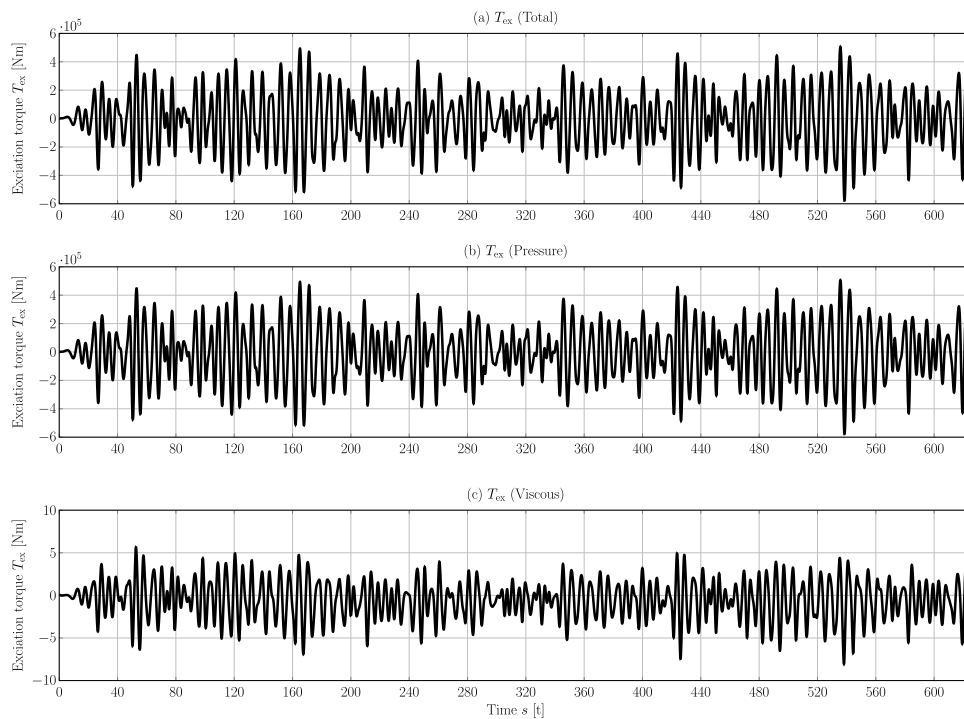
For the wave excitation test under irregular wave excitation, overall similar results as for the previous cases are found. By way of example, Fig. 13(a)–(c) show the time traces for the total wave excitation torque T_{ex} and its pressure and

Table 15
nRMSD [%] between the scales for the pressure excitation torque.

	1/5 _F	1/5 _{FaR}	1/20 _F	1/20 _{FaR}
1/1	0.07	0.07	0.15	0.13
1/5 _F		0.02	0.19	0.19
1/5 _{FaR}			0.20	0.19
1/20 _F				0.09

Table 16
nRMSD [%] between the scales for the viscous excitation torque.

	1/5 _F	1/5 _{FaR}	1/20 _F	1/20 _{FaR}
1/1	352.73	0.14	2912.60	0.11
1/5 _F		352.73	2560.70	352.67
1/5 _{FaR}			2912.60	0.22
1/20 _F				2912.50

**Fig. 13.** Time trace of the excitation torque for the irregular sea state at 1/1 scale: (a) Total T_{ex} ; (b) Pressure T_{ex} ; (c) Viscous T_{ex} .

viscous shear components, respectively. As for the case of regular wave excitation, the total T_{ex} is dominated by the pressure component, while the viscous component of T_{ex} is several orders of magnitude lower.

The SDF of the total T_{ex} , and its viscous component, are shown in Figs. 14(a) and (b), respectively. As expected from the results of the regular wave excitation, qualitatively, no differences can be observed for the total T_{ex} , while the viscous component of T_{ex} at 1/20_F scale is significantly larger.

These results are underpinned by the quantitative analysis based on the nRMSD. Results for the nRMSD between the total and viscous excitation torque (in the time domain) are listed in Tables 17 and 18.

For the total excitation torque, the results are consistent with the previous results, showing nRMSD values of < 0.1%. Similarly, for the viscous component of T_{ex} , relatively large values of up to $\sim 1300\%$ are calculated for the nRMSD. Inspection of the deviation between the scales reveals the same phenomena as for the regular wave excitation test, whereby the viscosity and, thus, the according T_{ex} is larger at the Froude scales. Good agreement between the viscous T_{ex} is achieved when Reynolds and Froude scaling is obeyed. Ultimately, the influence of the viscous component on the total T_{ex} is negligible.

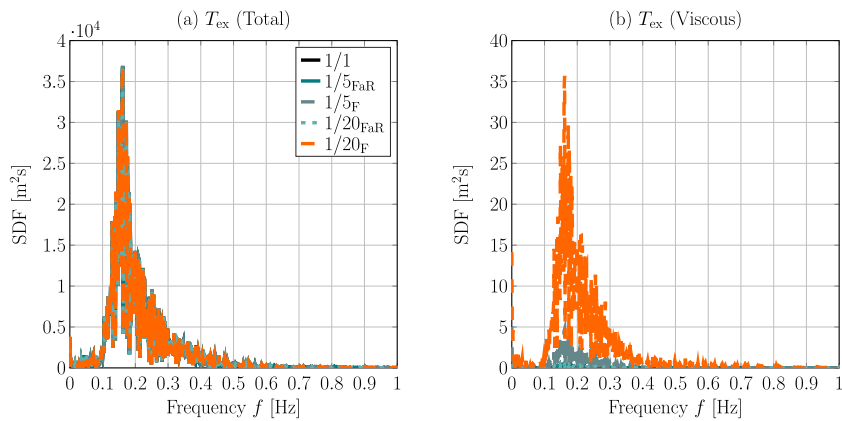


Fig. 14. SDF of the excitation torque for the irregular sea state: (a) Total T_{ex} ; (b) Viscous T_{ex} .

Table 17

nRMSD [%] between the scales for the total excitation torque.

	1/5 _F	1/5 _{FaR}	1/20 _F	1/20 _{FaR}
1/1	0.05	0.04	0.08	0.04
1/5 _F		0.05	0.06	0.04
1/5 _{FaR}			0.07	0.04
1/20 _F				0.06

Table 18

nRMSD [%] between the scales for the viscous excitation torque.

	1/5 _F	1/5 _{FaR}	1/20 _F	1/20 _{FaR}
1/1	168.25	0.40	1363.25	0.55
1/5 _F		168.32	1974.03	168.27
1/5 _{FaR}			1363.62	0.46
1/20 _F				1363.58

Table 19

nRMSD [%] between the scales for the PTO piston length.

	1/5 _F	1/5 _{FaR}	1/20 _F	1/20 _{FaR}
1/1	0.14	0.15	0.12	0.00
1/5 _F		0.02	0.22	0.14
1/5 _{FaR}			0.24	0.15
1/20 _F				0.12

Table 20

nRMSD [%] between the scales for the total T_{Hyd} .

	1/5 _F	1/5 _{FaR}	1/20 _F	1/20 _{FaR}
1/1	0.11	0.12	0.11	0.00
1/5 _F		0.01	0.20	0.11
1/5 _{FaR}			0.21	0.12
1/20 _F				0.11

5.3. Free decay test

Figs. 15(a)–(b) show the free decay results for the WEC displacement (by means of the displacement of the PTO translator shaft L_{PTO}), the total hydrodynamic torque, T_{Hyd} , and its viscous component, as well as the SDF based on L_{PTO} , respectively. For the quantitative analysis, nRMSD values are listed in Tables 19–22.

As for the previous cases, the qualitatively and quantitatively largest deviations between scales can be observed for the viscous component of the hydrodynamic force (nRMSD up to $\sim 1400\%$). From the free decay test, it can be observed that the deviation in the viscous component of the hydrodynamic force has not only a negligible influence on the total hydrodynamic force (max. nRMSD $< 0.25\%$) but also, as expected, negligible influence on the device motion (max. nRMSD for $L_{PTO} < 0.25\%$ and $\ll 0.25\%$ for the SDF).

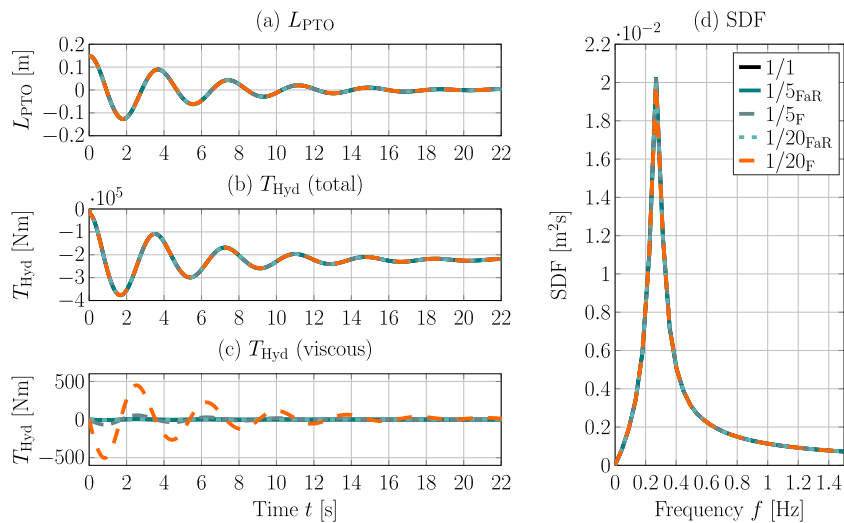


Fig. 15. Time trace of (a) the WEC displacement, (b) the total hydrodynamic torque and (c) the viscous component of the hydrodynamic torque. (d) shows the SDF based on L_{PTO} .

Table 21
nRMSD [%] between the scales for the viscous T_{Hyd} .

	1/5 _F	1/5 _{FaR}	1/20 _F	1/20 _{FaR}
1/1	170.70	2.80	1389.83	0.03
1/5 _F		170.13	1221.74	170.67
1/5 _{FaR}			1389.64	2.80
1/20 _F				1389.80

Table 22
nRMSD [%] between the scales for the SDF based on L_{PTO} .

	1/5 _F	1/5 _{FaR}	1/20 _F	1/20 _{FaR}
1/1	0.02	0.03	0.03	0.00
1/5 _F		0.00	0.05	0.02
1/5 _{FaR}			0.05	0.03
1/20 _F				0.03

Table 23
nRMSD [%] between the scales for the WEC displacement.

	1/5 _F	1/5 _{FaR}	1/20 _F	1/20 _{FaR}
1/1	0.03	0.02	0.08	0.02
1/5 _F		0.01	0.06	0.01
1/5 _{FaR}			0.07	0.01
1/20 _F				0.07

5.4. Forced oscillation tests

In the following, forced oscillation tests with single- and multi-frequency excitation are discussed.

5.4.1. Single-frequency excitation

Figs. 16(a)–(c) show the time trace of the phase averaged WEC displacement, the total hydrodynamic torque, and the viscous component of the total hydrodynamic torque, respectively. The corresponding ‘deviation matrices’ are shown in Tables 23–25. Overall, similar results as for all previous test cases are found for the single-frequency forced oscillation test. If Froude and Reynolds similarity is achieved, all considered quantities scale correctly (nRMSD < 0.6%, see Tables 23–25). If only Froude similarity is achieved, viscous forces on the WEC hull are larger if only Froude scaling is considered (nRMSD > 155%, see Table 25); however, with no effect on the overall loads on the WEC hull or WEC motion.

5.4.2. Multi-frequency excitation

Figs. 17(a)–(d) show the time trace of the WEC displacement, the total hydrodynamic torque, the viscous component of the total hydrodynamic torque, L_{PTO} SDF, respectively. The corresponding ‘deviation matrices’ are shown in Tables 26–29.

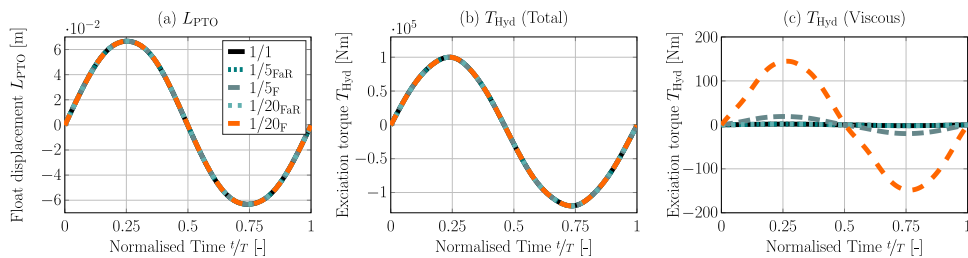


Fig. 16. Time trace of the phase averaged (a) WEC displacement, (b) total hydrodynamic torque, and (c) viscous component of the total hydrodynamic torque.

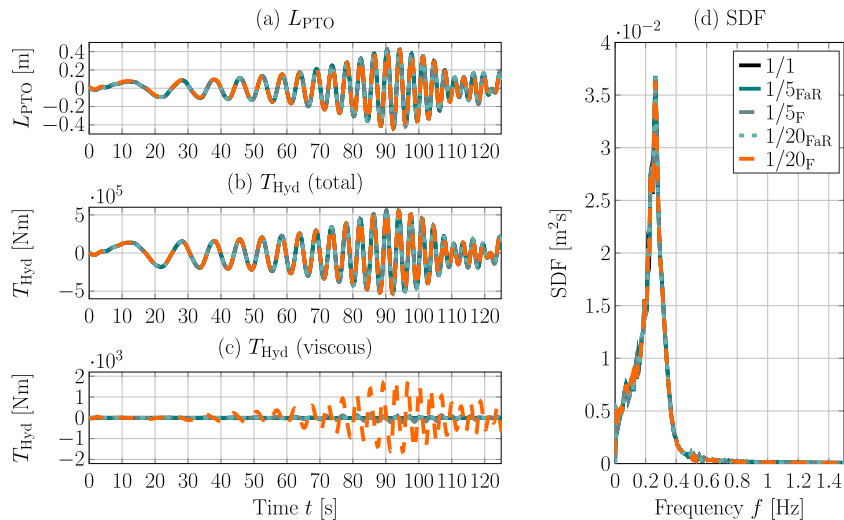


Fig. 17. Time trace of (a) the WEC displacement, (b) the total hydrodynamic torque and (c) the viscous component of the hydrodynamic torque. (d) shows the L_{PTO} SDF.

Table 24
nRMSD [%] between the scales for the total excitation torque.

	1/5 _F	1/5 _{FaR}	1/20 _F	1/20 _{FaR}
1/1	0.04	0.03	0.05	0.03
1/5 _F		0.00	0.02	0.01
1/5 _{FaR}			0.02	0.01
1/20 _F				0.02

Table 25
nRMSD [%] between the scales for the viscous excitation torque.

	1/5 _F	1/5 _{FaR}	1/20 _F	1/20 _{FaR}
1/1	346.02	0.59	2825.42	0.43
1/5 _F		346.07	2480.00	346.00
1/5 _{FaR}			2825.45	0.19
1/20 _F				2825.80

From an inspection of Fig. 17(a)–(c), larger displacement and force magnitudes can be observed, compared to the single-frequency excitation (multiplication factor ~ 7) case. This is expected since the multi-frequency excitation used herein results in resonance excitation of the WEC (see Fig. 17(c) and Fig. 15(d)). The observed scaling effects are relatively consistent with the results for the single-frequency forced oscillation test and, in fact, with all previous results. Slightly larger deviations, compared to the single-frequency excitation, can be found for the PTO piston length and the total excitation torque. These larger deviations may be due to the larger displacement and force magnitudes. However, overall, the deviations between the scales for L_{PTO} (and the according SDF) and the total hydrodynamic torques can still be considered negligible.

Table 26
nRMSD [%] between the scales for the PTO piston length.

	1/5 _F	1/5 _{FaR}	1/20 _F	1/20 _{FaR}
1/1	0.20	0.20	0.67	0.16
1/5 _F		0.02	0.67	0.05
1/5 _{FaR}			0.67	0.05
1/20 _F				0.66

Table 27
nRMSD [%] between the scales for the total excitation torque.

	1/5 _F	1/5 _{FaR}	1/20 _F	1/20 _{FaR}
1/1	0.19	0.19	0.18	0.15
1/5 _F		0.02	0.15	0.04
1/5 _{FaR}			0.17	0.05
1/20 _F				0.14

Table 28
nRMSD [%] between the scales for the viscous excitation torque.

	1/5 _F	1/5 _{FaR}	1/20 _F	1/20 _{FaR}
1/1	156.86	0.25	1320.10	0.20
1/5 _F		156.86	1163.40	156.84
1/5 _{FaR}			1320.10	0.10
1/20 _F				1320.10

Table 29
nRMSD [%] between the scales for the SDF.

	1/5 _F	1/5 _{FaR}	1/20 _F	1/20 _{FaR}
1/1	0.03	0.04	0.10	0.03
1/5 _F		0.00	0.10	0.01
1/5 _{FaR}			0.10	0.01
1/20 _F				0.09

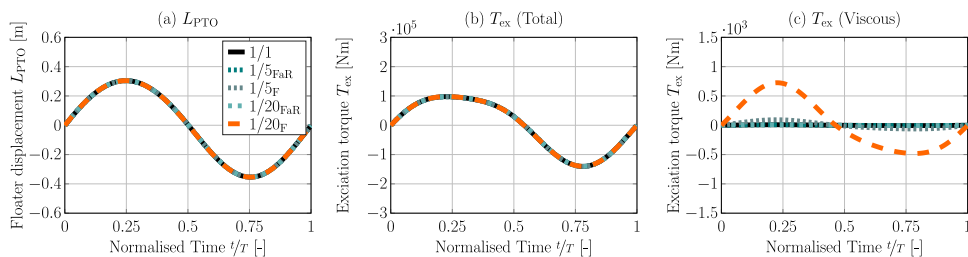


Fig. 18. Time trace of the phase averaged (a) the WEC displacement, (b) the total hydrodynamic torque, and (c) the viscous component of the total hydrodynamic torque.

5.5. Wave-induced WEC motion tests

Finally, wave-induced WEC motion, under regular and irregular wave excitation, is analysed.

5.5.1. Regular waves

Fig. 18(a)–(c) show the time trace of the phase averaged WEC displacement, the total excitation torque, and the viscous component of the total excitation torque. The ‘deviation matrices’ are shown in Tables 30–32.

The magnitude of the WEC displacement (Fig. 18(a)) is of a similar order as for the multi-frequency forced oscillation test, while the total excitation torque (Fig. 18(b)) is slightly lower. Similarly, the viscous component of the excitation torque (Fig. 18(c)) is slightly lower, compared to the multi-frequency forced oscillation test. Overall, qualitatively and quantitatively, the deviations between the scales are consistent with the previous test cases.

5.5.2. Regular waves – resonance

As stated in Section 3, to analyse the hydrodynamic scaling effects under controlled conditions, the wave period of the regular wave is chosen to match the natural frequency of the device, taken from the peak of the SDF plot in Fig. 15(d).

Table 30
nRMSD [%] between the scales for the WEC displacement.

	1/5 _F	1/5 _{FaR}	1/20 _F	1/20 _{FaR}
1/1	0.03	0.04	0.08	0.01
1/5 _F		0.02	0.10	0.03
1/5 _{FaR}			0.12	0.04
1/20 _F				0.08

Table 31
nRMSD [%] between the scales for the total excitation torque.

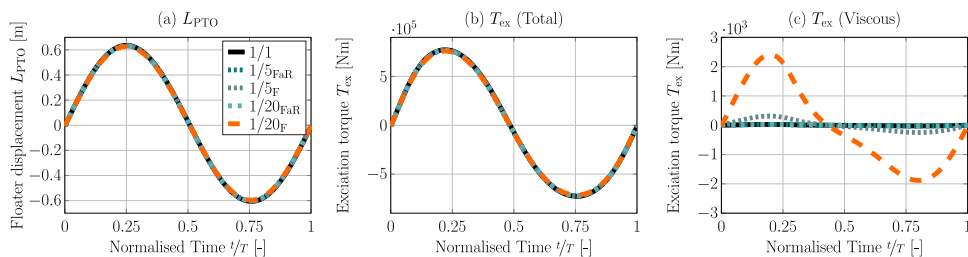
	1/5 _F	1/5 _{FaR}	1/20 _F	1/20 _{FaR}
1/1	0.07	0.15	0.11	0.06
1/5 _F		0.11	0.14	0.08
1/5 _{FaR}			0.22	0.12
1/20 _F				0.14

Table 32
nRMSD [%] between the scales for the viscous excitation torque.

	1/5 _F	1/5 _{FaR}	1/20 _F	1/20 _{FaR}
1/1	354.47	0.09	2968.60	0.12
1/5 _F		354.45	2641.10	354.42
1/5 _{FaR}			2968.50	0.16
1/20 _F				2968.51

Table 33
nRMSD [%] between the scales for the WEC displacement.

	1/5 _F	1/5 _{FaR}	1/20 _F	1/20 _{FaR}
1/1	0.21	0.23	0.60	0.30
1/5 _F		0.03	0.43	0.13
1/5 _{FaR}			0.43	0.15
1/20 _F				0.30

**Fig. 19.** Time trace of the phase averaged (a) the WEC displacement, (b) the total hydrodynamic torque, and (c) the viscous component of the total hydrodynamic torque.

The results of the phase averaged WEC displacement, the total excitation torque, and the viscous component of the total excitation torque are shown in Fig. 19(a)–(c).

Comparing the results shown in Fig. 19(a)–(c) for the resonance case with the results shown in Fig. 18(a)–(c), it can readily be seen that the device motion, indicated by L_{PTO} , as well as the excitation torques are increased. Furthermore, from a qualitative inspection, slightly different trajectories in the excitation torque can be observed. However, in qualitative terms, the deviations between the scale for the WEC displacement and the excitation torque for the case of resonance excitation follow the same trend as the previous test cases.

For a quantitative analysis, Tables 33–35 list the nRMSD values for the WEC displacement, the total excitation force, and its viscous component, respectively. Comparing the quantitative results for the resonance excitation case with the results for regular excitation (see Tables 30–32), it can be observed that, for the viscous component of the excitation torque, similar differences between the scales can be observed for the resonance and regular excitation cases. For the total excitation torque, differences between the scales are approximately twice as large for the case of resonance excitation, compared with the regular excitation test. For the WEC displacement, the differences between the scales are approximately one order of magnitude larger for the case of resonance excitation, compared with the regular excitation test.

To analyse the potential source of the larger excursions in the WEC displacement and the total excitation torque in the case of the resonance excitation, compared to the regular excitation, the flow field, by means of the pressure and the

Table 34
nRMSD [%] between the scales for the total excitation torque.

	$1/5_F$	$1/5_{FaR}$	$1/20_F$	$1/20_{FaR}$
1/1	0.26	0.28	0.64	0.33
$1/5_F$		0.04	0.45	0.18
$1/5_{FaR}$			0.46	0.21
$1/20_F$				0.33

Table 35
nRMSD [%] between the scales for the viscous excitation torque.

	$1/5_F$	$1/5_{FaR}$	$1/20_F$	$1/20_{FaR}$
1/1	329.75	0.39	2752.20	0.17
$1/5_F$		329.53	2422.50	329.67
$1/5_{FaR}$			2752.00	0.23
$1/20_F$				2752.10

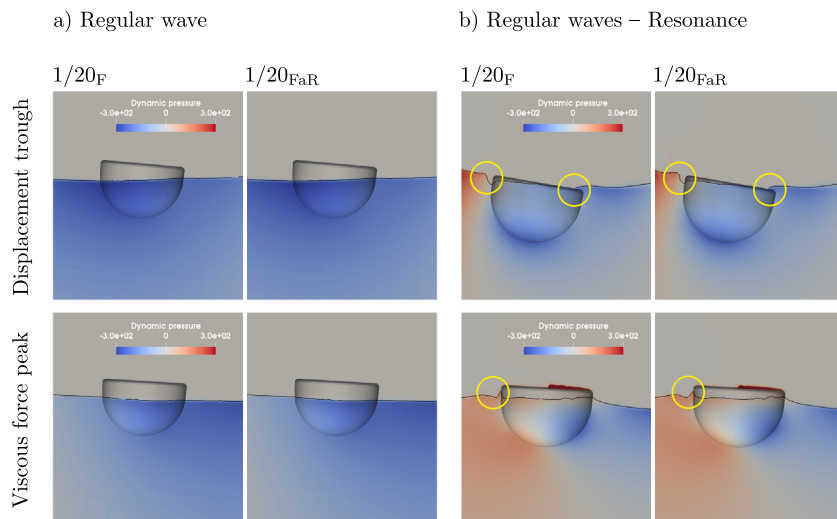


Fig. 20. Pressure field around the WEC structure for (a) the ‘regular’ and (b) the resonance excitation. The sub-figures in the top row refer to a time instance at which the WEC structure shows a trough in the displacement. The bottom row of the sub-figures refers to a time instance where the viscous force component shows a peak.

velocity field, is analysed. In the following, results for the resonance and non-resonant regular excitation are compared for the $1/20_F$ and the $1/20_{FaR}$ scales, showing relatively large differences.

Fig. 20(a) and (b) show the pressure field around the WEC structure for the both regular non-resonant and the regular resonance excitation, respectively. The sub-figures in the top row refer to a time instance at which the WEC structure shows a trough in displacement. The bottom row of the sub-figures refers to a time instance where the viscous force component shows a peak and, thus, relatively large differences between the scales.

For the case of regular non-resonant excitation, virtually no differences are visible in the pressure field, as well as the free surface elevation. To enhance the visibility of potential differences, the colour range for the pressure field has been changed, showing only negative pressure values, in Fig. 21. However, even in Fig. 21, no differences are visible, underlining the results found in Section 5.5.1.

Comparing the pressure field for the case of resonance excitation, in Fig. 20(b), to the case of non-resonant excitation, a larger system response is visible (consistent with the phase averaged time traces), leading to overtopping of the device.

Comparing the pressure field between the $1/20_F$ and the $1/20_{FaR}$ scale for the case of resonance excitation, again, no striking differences are visible. However, inspecting the free surface elevation, slight differences between the $1/20_F$ and the $1/20_{FaR}$ scale can be observed, highlighted by the yellow circles. These visible differences, due to radiation/diffraction effects, are the likely cause of the larger differences between the scales for the case of the resonance excitation, compared to the regular excitation.

For completeness, the screen shots of the velocity field around the WEC structure are shown in Fig. 22(a) and (b) for the regular and the resonance excitation, respectively. The sub-figures in the top row refer to a time instance at which the WEC structure shows a trough in the displacement. The bottom row of the sub-figures refers to a time instance where the viscous force component shows a peak. Similar to the pressure field, the velocity field for the regular excitation cases

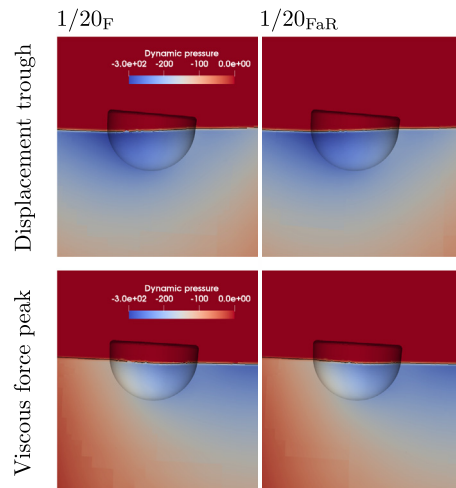


Fig. 21. Pressure field around the WEC structure for the ‘regular’ excitation, only showing negative pressure values. The sub-figures in the top row refer to a time instance at which the WEC structure shows a trough in the displacement. The bottom row of the sub-figures refers to a time instance where the viscous force component shows a peak.

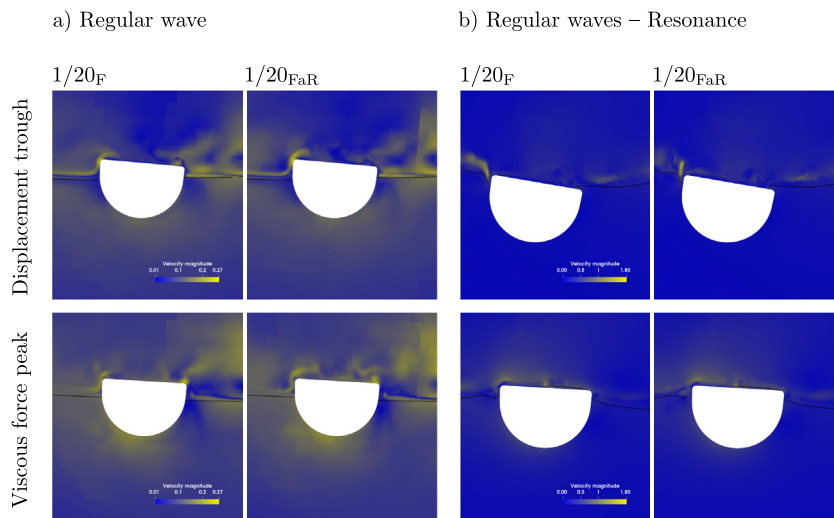


Fig. 22. Screen shots of the velocity field around the WEC structure for (a) the ‘regular’ and (b) the resonance excitation, respectively. The sub-figures in the top row refer to a time instance at which the WEC structure shows a trough in the displacement. The bottom row of the sub-figures refers to a time instance where the viscous force component shows a peak.

do not show notable differences between the scales. For the resonance excitation, only differences for the velocity of the air are visible between the scales, induced by the differences in the free surface elevation.

5.5.3. Irregular waves

Finally, wave-induced motion for the case of irregular wave excitation is considered. Fig. 23(a)–(d) show the SDF of the WEC displacement, the total excitation torque, the viscous component of the excitation torque, and a snippet (between 300–400 s) of the time trace of the WEC displacement, respectively. The results of the corresponding quantitative analysis are shown in Tables 36–38. Overall, the qualitative and quantitative results are consistent with the findings of all previous test cases.

6. Discussion

For the particular test cases in this study, the presented results in Section 5 generally indicate negligible influence of hydrodynamic scaling effects on the waves/environment, the WEC displacement, and the total hydrodynamic/excitation torque.

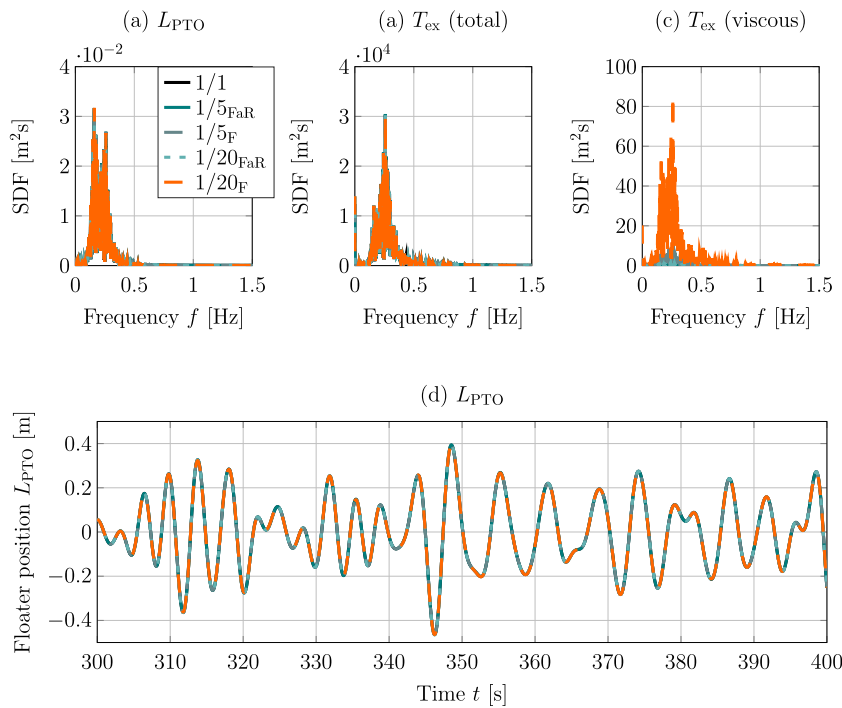


Fig. 23. SDF of (a) the WEC displacement, (b) the total excitation torque, and (c) the viscous component of the excitation torque. (d) Shows a snippet (between 300–400 s) of the time trace of the WEC displacement.

Table 36
nRMSD [%] between the scales for the WEC displacement.

	1/5 _F	1/5 _{FaR}	1/20 _F	1/20 _{FaR}
1/1	0.01	0.01	0.01	0.01
1/5 _F		0.00	0.02	0.01
1/5 _{FaR}			0.02	0.01
1/20 _F				0.01

Table 37
nRMSD [%] between the scales for the total excitation torque.

	1/5 _F	1/5 _{FaR}	1/20 _F	1/20 _{FaR}
1/1	0.01	0.03	0.03	0.02
1/5 _F		0.02	0.03	0.02
1/5 _{FaR}			0.02	0.01
1/20 _F				0.02

Table 38
nRMSD [%] between the scales for the viscous excitation torque.

	1/5 _F	1/5 _{FaR}	1/20 _F	1/20 _{FaR}
1/1	25.98	2.34	200.91	2.34
1/5 _F		23.64	174.94	23.64
1/5 _{FaR}			198.58	0.04
1/20 _F				198.57

Considering the input waves in this study, which is focussed on operational conditions, the waves have a relatively modest slope and virtually negligible non-linearity, verified by the excellent agreement observed between the different scales for both the free surface and the wave kinematics. On the one hand, investigating steeper waves with a range of different wave heights may reveal an influence of hydrodynamic scaling effects on the input waves/environment. However, on the other hand, reducing the potential scaling effects on the environment allows a focus on the investigation of the fluid–structure interaction. For this reason, the distance between the wave generation boundary and the device is

relatively short, to reduce the influence of artificial numerical dissipation in the wave propagation, which might introduce a scale dependence that is an artefact of the CFD simulations only.

Regarding the fluid–structure interaction, some observations can be made. The wave excitation force tests reveal a slightly more noticeable scale dependence when including a structure and analysing the hydrodynamic loads, compared to the relative scale independence of the wave only case. With the results shown in [Tables 14–16](#) the cause for the differences between the scales can be allocated to the significant scale dependence of the viscous load component. For the case of wave driven device motion, the fluid–structure interaction shows hydrodynamic scale effects dependent on the device motion amplitude. In the case of resonance excitation, the results reveal noticeable differences in the free surface profile around the structure, which are likely induced by a scale dependence of the diffracted/radiated wave field, considering the scale independence of the input waves.

In the context of the reviewed literature (see [Section 1.2](#)) the results discussed herein are consistent with previous findings. [Gu et al. \(2018\)](#) and [Wei et al. \(2013, 2015\)](#) find that viscous effects are influenced by scaling effects. However, [Wei et al. \(2013, 2015\)](#) also point out that the differences between scales is outweighed by scale independent driving forces. For a device like a flap type OWSC, these results are indeed surprising (also in the light of the findings by [Schmitt and Elsässer, 2017b](#)), since (shape induced) viscous forces are, in contrast to a device like the Wavestar, assumed to be significant. For the analysis procedure proposed by [Zabala et al. \(2019\)](#), the scale independence of the hydrodynamic effects for the Wavestar device, and likely all similar, heave-dominated, devices with hemispherical bottom shapes, is important. With the underlying assumption of the methodology that a validated small-scale NWT setup is also valid at full-scale, the presented results in [Section 5](#) prove the feasibility of the proposed methodology.

7. Conclusions

Avoiding mechanical scaling effects, such as excessive friction, and providing the ability to achieve Froude and Reynold similarity, CFD-based NWTs are powerful tools to analyse the hydrodynamic scaling effects on WEC devices. Based on a validated numerical model, this study analyses hydrodynamic scale effects for the Wavestar WEC device. Following an incremental procedure with progressively increasing complexity of the considered test cases, the study covers the full range of relevant test cases for WEC applications.

From the results, the straightforward conclusion can be drawn that for the Wavestar device, and likely all similar, heave-dominated, devices with hemispherical bottom shapes, hydrodynamic scaling effects are negligible for the overall WEC dynamics and total loads on the hull. Even when Froude and Reynolds similarity are not obeyed simultaneously, the deviations across scales fall well below 1%. Only the viscous shear component of the excitation torque showed significant deviations across scales only when Froude and Reynolds similarity are obeyed simultaneously, scaling effects can be ruled out for the viscous component. However, as stated throughout the study, the observed deviations do not influence the total load and WEC displacement. Thus, for devices whose dynamics and loads are mainly driven by pressure induced forces, hydrodynamic scaling effects in operational conditions can be assumed negligible. It should be noted that, in order to analyse the scaling effects in extreme conditions, including e.g. breaking waves, quite a different, separate, study is required.

The observed scale independence in operational conditions has implication for the design of physical wave tank tests. Since the well-known problem of a correct Froude and Reynolds scaling in physical wave tanks does not seem to affect the overall device dynamics, scaling effects in physical wave tanks are mainly driven by mechanical artefacts, such are exaggerated friction in bearings or PTO components. Thus, to avoid scaling effects in physical tests, effort should be made to reduce such mechanical artefacts.

CRedit authorship contribution statement

Christian Windt: Conceptualization, Data curation, Formal analysis, Investigation, Methodology, Software, Visualization, Roles/Writing - original draft, Writing - review & editing. **Josh Davidson:** Conceptualization, Data curation, Formal analysis, Investigation, Methodology, Roles/Writing - original draft, Writing - review & editing. **John V. Ringwood:** Funding acquisition, Project administration, Supervision, Writing - review & editing.

Declaration of competing interest

The authors declare that they have no known competing financial interests or personal relationships that could have appeared to influence the work reported in this paper.

Acknowledgements

This paper is based upon work supported by Science Foundation Ireland under Grant No. 13/IA/1886. The research reported in this paper has also been supported by the NRD Funds (TKP2020 IES, Grant No. BME-IE-WAT) and (TKP2020 NC, Grant No. BME-NCS) based on the charter of bolster issued by the NRD Office under the auspices of the Ministry

for Innovation and Technology. This project has received funding from the European Union's Horizon 2020 research and innovation programme under the Marie Skłodowska-Curie grant agreement number 867453.

Appendix. Time step analysis

To analyse the influence of a scaled time step size on the results of the surface elevation and the WEC dynamics, simulations with a time step of 0.001 s for all scales and well as with scaled time steps are performed.

Fig. A.24(a) and (b) show the time traces of the free surface elevation at WP4 for a fixed time step size of 0.001 s and a scaled time step size at 1/1 scale and 1/5_{FaR} scale, scale. The same data is plotted for the irregular waves in Fig. A.25(a) and (b). Finally, Fig. A.26(a) and (b) show the time traces of the WEC displacement and the excitation torque, respectively, for a fixed time step size of 0.001 s and a scaled time step size at 1/1 scale. From the plotted results, no influence of the time step size on the simulation results can be identified. Thus, for computational efficiency, scaled time step sizes are used throughout this study.

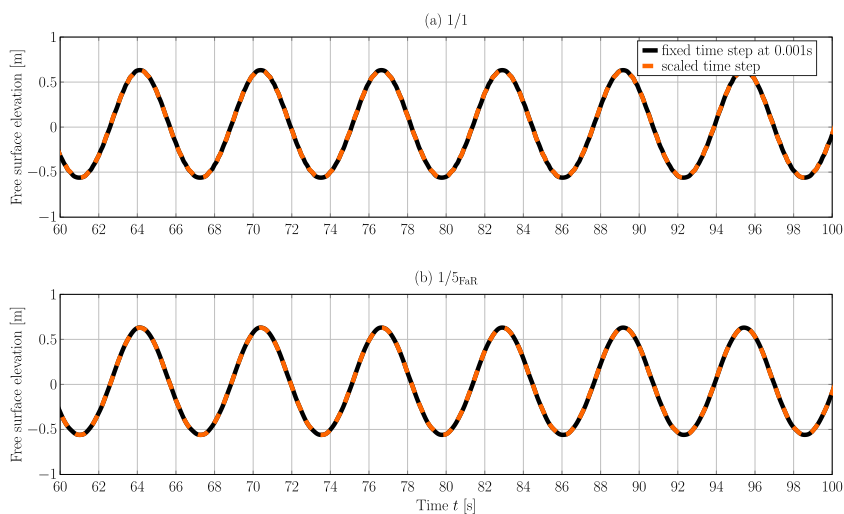


Fig. A.24. Time traces of the free surface elevation at WP4 for a fixed time step size of 0.001 s and a scaled time step size at (a) 1/1 scale and (b) 1/5_{FaR} scale.

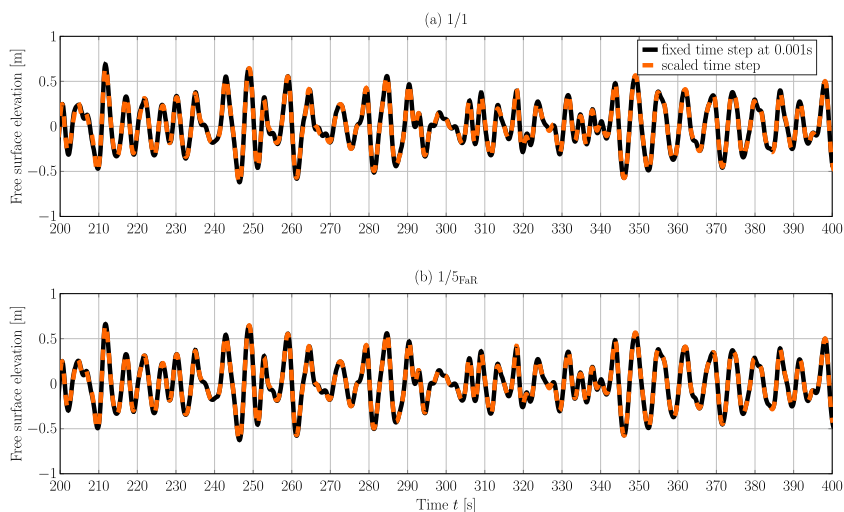


Fig. A.25. Time traces of the free surface elevation at WP4 for a fixed time step size of 0.001 s and a scaled time step size for (a) 1/1 scale and (b) 1/5_{FaR} scale.

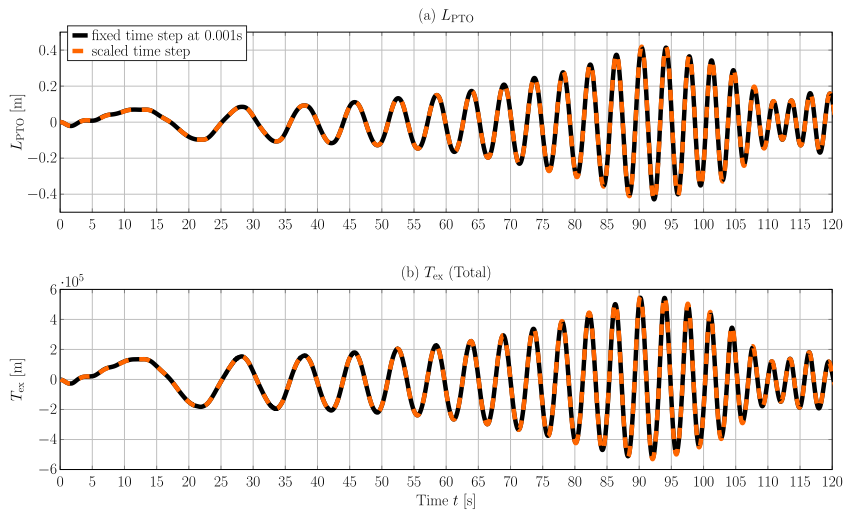


Fig. A.26. Time traces of the (a) WEC displacement and (b) the excitation torque for a fixed time step size of 0.001 s and a scaled time step size at 1/1 scale.

References

- ANSYS, 2020. ANSYS AQWA product website. <https://www.ansys.com/products/structures/ansys-aqwa>. (Accessed 14 April 2020).
- Babart, A., 2015. A database of capture width ratio of wave energy converters. *Renew. Energy* 80, 610–628.
- Berberović, E., van Hinsberg, N.P., Jakirlić, S., Roisman, I.V., Tropea, C., 2009. Drop impact onto a liquid layer of finite thickness: Dynamics of the cavity evolution. *Phys. Rev. E* 79, 036306–1–15.
- Dai, S., Day, S., Yuan, Z., Wang, H., 2019. Investigation on the hydrodynamic scaling effect of an OWC type wave energy device using experiment and CFD simulation. *Renew. Energy* 142, 184–194.
- Davidson, J., Costello, R., 2020. Efficient nonlinear hydrodynamic models for wave energy converter design—A scoping study. *J. Mar. Sci. Eng.* 8 (1), 35.
- Davidson, J., Giorgi, S., Ringwood, J.V., 2016. Identification of wave energy device models from numerical wave tank data—Part 1: Numerical wave tank identification tests. *IEEE Trans. Sustain. Energy* 7 (3), 1012–1019.
- Davidson, J., Windt, C., Giorgi, G., Genest, R., Ringwood, J.V., 2019. Evaluation of energy maximising control systems for wave energy converters using OpenFOAM. In: *OpenFOAM®*. Springer, pp. 157–171.
- de O. Falcão, A.F., 2010. Wave energy utilization: A review of the technologies. *Renew. Sustain. Energy Rev.* 14, 899–918.
- Elhanafi, A., 2016. Prediction of regular wave loads on a fixed offshore oscillating water column-wave energy converter using CFD. *J. Ocean Eng. Sci.* 1 (4), 268–283.
- Elhanafi, A., Kim, C.J., 2018. Experimental and numerical investigation on wave height and power take-off damping effects on the hydrodynamic performance of an offshore-stationary OWC wave energy converter. *Renew. Energy* 125, 518–528.
- Elhanafi, A., Macfarlane, G., Fleming, A., Leong, Z., 2017a. Experimental and numerical measurements of wave forces on a 3D offshore stationary OWC wave energy converter. *Ocean Eng.* 144, 98–117.
- Elhanafi, A., Macfarlane, G., Fleming, A., Leong, Z., 2017b. Investigations on 3D effects and correlation between wave height and lip submergence of an offshore stationary OWC wave energy converter. *Appl. Ocean Res.* 64, 203–216.
- Elhanafi, A., Macfarlane, G., Fleming, A., Leong, Z., 2017c. Numerical hydrodynamic analysis of an offshore stationary-floating oscillating water column-wave energy converter using CFD. *Int. J. Naval Archit. Ocean Eng.* 9, 77–99.
- Elhanafi, A., Macfarlane, G., Fleming, A., Leong, Z., 2017d. Scaling and air compressibility effects on a three-dimensional offshore stationary OWC wave energy converter. *Appl. Energy* 189, 1–20.
- Elhanafi, A., Macfarlane, G., Fleming, A., Leong, Z., 2017e. Underwater geometrical impact on the hydrodynamic performance of an offshore oscillating water column-wave energy converter. *Renew. Energy* 105, 209–231.
- Elhanafi, A., Macfarlane, G., Ning, D., 2018. Hydrodynamic performance of single-chamber and dual-chamber offshore-stationary oscillating water column devices using CFD. *Appl. Energy* 228, 82–96.
- Folley, M., 2016. *Numerical Modelling of Wave Energy Converters: State-of-the-Art Techniques for Single Devices and Arrays*. Academic Press.
- García-Violini, D., Peña Sanchez, Y., Faedo, N., Windt, C., Ferri, F., Ringwood, J., 2021. Experimental implementation and validation of a broadband LTI energy-maximizing control strategy for the Wavestar device. *IEEE Trans. Control Syst. Technol.* Early Access.
- Giorgi, G., Ringwood, J., 2017. Nonlinear Froude-Krylov and viscous drag representations for wave energy converters in the computation/fidelity continuum. *Ocean Eng.* 141, 164–175.
- Gu, H., Stansby, P., Stallard, T., Moreno, E., 2018. Drag, added mass and radiation damping of oscillating vertical cylindrical bodies in heave and surge in still water. *J. Fluids Struct.* 82, 343–356.
- Hals, J., Babart, A., Krokstad, J., Muliawan, M.J., Kurniawan, A., Moan, T., 2015. The NumWEC project. Numerical estimation of energy delivery from a selection of wave energy converters. Tech. Rep., Norwegian University of Science and Technology.
- Heller, V., 2011. Scale effects in physical hydraulic engineering models. *J. Hydraul. Res.* 49 (3), 293–306.
- Higuera, P., Lara, J.L., Losada, I.J., 2013. Realistic wave generation and active wave absorption for Navier–Stokes models application to OpenFOAM. *Coast. Eng.* 71, 102–118.
- Hirt, C.W., Nichols, B.D., 1981. Volume of fluid (VOF) method for the dynamics of free boundaries. *J. Comput. Phys.* 39, 201–225.
- Holzmann, T., 2016. *Mathematics, Numerics, Derivations and OpenFOAM*. Holzmann CFD.
- Issa, R.I., 1986. Solution of the implicitly discretised fluid flow equation by operator-splitting. *J. Comput. Phys.* 62, 40–65.

- Jakobsen, M.M., 2014. Wave-structure Interactions on Point Absorber. Tech. Rep., Aalborg University Denmark.
- Jakobsen, M.M., Beatty, S., Iglesias, G., Kramer, M.M., 2016. Characterization of loads on a hemispherical point absorber wave energy converter. *Int. J. Mar. Energy* 13, 1–15.
- Menter, F., 1992a. Improved Two-equation $k-\omega$ Turbulence Models for Aerodynamic Flows. Tech. Rep., NASA Technical Memorandum TM-103975.
- Menter, F., 1992b. Performance of popular turbulence model for attached and separated adverse pressure gradient flows. *AIAA J.* 30 (8), 2066–2072.
- Menter, F., 1994. Two-equation eddy-viscosity turbulence models for engineering applications. *AIAA J.* 32 (8), 1598–1605.
- Menter, F., 1997. Eddy viscosity transport equations and their relation to the $k-\epsilon$ model. *J. Fluids Eng.* 119 (4), 876–884.
- Miquel, A., Kamath, A., Alagan Chella, M., Archetti, R., Bihs, H., 2018. Analysis of different methods for wave generation and absorption in a CFD-based numerical wave tank. *J. Mar. Sci. Eng.* 6 (2), 73.
- Mundon, T.R., Rosenberg, B.J., van Rij, J., 2017. Reaction body hydrodynamics for a multi-DOF point-absorbing WEC. In: *Proceedings of the 12th European Wave and Tidal Energy Conference, Cork*, pp. 997–1–10.
- Palm, J., Eskilson, C., Bergdahl, L., Bensow, R., 2018. Assessment of scale effects, viscous forces and induced drag on a point-absorbing wave energy converter by CFD simulations. *J. Mar. Sci. Eng.* 6, 124.
- Patankar, S., Spalding, D., 1972. A calculation procedure for heat, mass and momentum transfer in three-dimensional parabolic flows. *Int. J. Heat Mass Transfer* 15, 1787–1806.
- Penalba, M., Davidson, J., Windt, C., Ringwood, J.V., 2018. A high-fidelity wave-to-wire simulation platform for wave energy converters: Coupled numerical wave tank and power take-off models. *Appl. Energy* 226, 655–669.
- Ringwood, J., Davidson, J., Giorgi, S., 2016. Identifying models using recorded data. In: *Numerical Modelling of Wave Energy Converters*. Elsevier, pp. 123–147.
- Rusche, H., 2002. *Computational Fluid Dynamics of Dispersed Two-Phase Flows at High Phase Fractions* (Ph.D. thesis). Department of Mechanical Engineering, Imperial College London.
- Schmitt, P., Elsaesser, B., 2015. A review of wave makers for 3D numerical simulations. In: *Proceedings of the Computational Methods in Marine Engineering VI MARINE 2015, Rome, Italy*, pp. 437–446.
- Schmitt, P., Elsaesser, B., 2017a. The application of Froude scaling to model tests of oscillating wave surge converters. *Ocean Eng.* 141, 108–115.
- Schmitt, P., Elsaesser, B., 2017b. The application of Froude scaling to model tests of oscillating wave surge converters. *Ocean Eng.* 141, 108–115.
- Shalby, M., Elhanafi, A., Walker, P., Dorrell, D., 2019. CFD modelling of a small-scale fixed multi-chamber OWC device. *Appl. Ocean Res.* 88, 37–47.
- Tougaard, J., 2015. Underwater noise from a wave energy converter is unlikely to affect marine mammals. *PLoS One* 10 (7).
- Veritas, N., 2000. *Environmental Conditions and Environmental Loads*. Det Norske Veritas.
- Wei, Y., Rafiee, A., Dias, F., 2013. On the viscous effects in the interaction of water waves with an oscillating wave surge converter. In: *Proceedings of the 10th European Wave and Tidal Energy Conference, Aalborg*, pp. 808–1–9.
- Wei, Y., Rafiee, A., Henry, A., Dias, F., 2015. Wave interaction with an oscillating wave surge converter, Part I: Viscous effects. *Ocean Eng.* 104, 185–203.
- Weller, H.G., Tabor, G., Jasak, H., Fureby, C., 1998. A tensorial approach to computational continuum mechanics using object-oriented techniques. *Comput. Phys.* 12, 620–631.
- Windt, C., Davidson, J., Schmitt, P., Ringwood, J.V., 2019a. Contribution to the CCP-WSI blind test series 3: Analysis of scaling effects of moored point-absorber wave energy converters in a CFD-based numerical wave tank. In: *The 29th International Ocean and Polar Engineering Conference, International Society of Offshore and Polar Engineers*, pp. 3051–3058.
- Windt, C., Davidson, J., Ransley, E., Greaves, D., Jakobsen, M., Kramer, M., Ringwood, J., 2020a. Validation of a CFD-based numerical wave tank model for the power production assessment of the wavestar ocean wave energy converter. *Renew. Energy* 146, 2499–2516.
- Windt, C., Davidson, J., Ringwood, J., 2018. High-fidelity numerical modelling of ocean wave energy systems: A review of CFD-based numerical wave tanks. *Renew. Sustain. Energy Rev.* 93, 610–630.
- Windt, C., Davidson, J., Schmitt, P., Ringwood, J.V., 2019b. On the assessment of numerical wave makers for CFD simulations. *J. Mar. Sci. Eng.* 7 (2), 47.
- Windt, C., Faedo, N., Garcia-Violini, D., Peña Sanchez, Y., Ferri, F., Davidson, J., Ringwood, J.V., 2020b. Validation of a CFD-based numerical wave tank model of the 1/20th scale wavestar wave energy converter. *Fluids* 5 (3), 112.
- Zabala, I., Henriques, J., Blanco, J., Gomez, A., Gato, L., Bidaguren, I., Falcão, A., Amezaga, A., Gomes, R., 2019. Wave-induced real-fluid effects in marine energy converters: Review and application to OWC devices. *Renew. Sustain. Energy Rev.* 111, 535–549.